

1           Rapid whole brain imaging of neural activity in freely  
2                           behaving larval zebrafish (*Danio rerio*)

3

4   Lin Cong<sup>1,4</sup>, Zeguan Wang<sup>2,4</sup>, Yuming Chai<sup>2,4</sup>, Wei Hang<sup>1,4</sup>, Chunfeng Shang<sup>1</sup>, Wenbin  
5   Yang<sup>2</sup>, Lu Bai<sup>1</sup>, Jiulin Du<sup>1</sup>, Kai Wang<sup>1,3</sup>, Quan Wen<sup>2</sup>

6

7   1. Institute of Neuroscience, State Key Laboratory of Neuroscience, CAS Center for  
8       Excellence in Brain Science and Intelligence Technology, Chinese Academy of  
9       Sciences, Shanghai 200031, China.

10

11   2. Center for Integrative Imaging, Hefei National Laboratory for Physical Sciences at  
12       Microscale, CAS Center for Excellence in Brain Science and Intelligence Technology,  
13       University of Science and Technology of China, Hefei, 230027, China.

14

15   3. University of Chinese Academy of Sciences, Beijing 100049, China.

16

17   4. These authors contributed equally to this work.

18

19   Correspondence should be addressed to K.W. ([wangkai@ion.ac.cn](mailto:wangkai@ion.ac.cn)) or Q.W.  
20   ([qwen@ustc.edu.cn](mailto:qwen@ustc.edu.cn)).

21

22

23 **Abstract:**

24 The internal brain dynamics that link sensation and action are arguably better studied  
25 during natural animal behaviors. Here we report on a novel volume imaging and 3D  
26 tracking technique that monitors whole brain neural activity in freely swimming larval  
27 zebrafish (*Danio rerio*). We demonstrated the capability of our system through functional  
28 imaging of neural activity during visually evoked and prey capture behaviors in larval  
29 zebrafish.

30  
31

32 **Author Contributions**

33

34 K.W. and Q.W. conceived the project. K.W. conceived the idea of XLFM. L.C., Z.W.,  
35 W.H., L.B. and K.W. designed and built the XLFM. Y.C. Z.W. W.Y. and Q.W. designed  
36 and built the X-Y tracking and the real-time behavioral analysis system. L.C., Z.W., W.H.  
37 and K.W. designed and built the autofocus system. All authors worked collaboratively to  
38 integrate the XLFM and the tracking system together. C.S., J.D. and Q.W. designed  
39 zebrafish behavioral experiments. Y.C., Z.W., L.C. and W.H. did experiments under the  
40 supervision of C.S., J.D. K.W. and Q.W.. K.W and Q.W. wrote the paper with inputs  
41 from all authors.

42

43 **Main text:**

44 **Introduction:**

45 A central goal in systems neuroscience is to understand how distributed neural circuitry  
46 dynamics drive animal behaviors. The emerging field of optical neurophysiology allows  
47 the monitoring [1, 2] and manipulating [3-5] of the activities of defined populations of  
48 neurons that express genetically encoded activity indicators [6, 7] and light-activated  
49 proteins [1, 4, 5, 8]. Larval zebrafish (*Danio rerio*) are an attractive model system to  
50 investigate the neural correlates of behaviors owing to their small brain size, optical  
51 transparency, and rich behavioral repertoire [9, 10]. Whole brain imaging of larval  
52 zebrafish using light sheet/two-photon microscopy holds considerable potential in  
53 creating a comprehensive functional map that links neuronal activities and behaviors [11-  
54 13].

55

56 Recording neural activity maps in larval zebrafish has been successfully integrated with  
57 the virtual reality paradigm: closed-loop fictive behaviors in immobilized fish can be  
58 monitored and controlled via visual feedback that varies according to the electrical output  
59 patterns of motor neurons [11, 14]. The behavioral repertoire, however, may be further  
60 expanded in freely swimming zebrafish whose behavioral states can be directly inferred  
61 and when sensory feedback loops are mostly intact and active. For example, it is likely  
62 that vestibular as well as proprioceptive feedbacks are perturbed in immobilized zebrafish  
63 [14, 15]. The crowning moment during hunting behavior [16-18] — when a fish succeeds  
64 in catching a paramecium — cannot be easily replicated in a virtual reality setting.

65 Therefore, whole brain imaging in a freely swimming zebrafish may allow optical  
66 interrogation of brain circuits underlying a range of less explored behaviors.

67

68 Although whole brain functional imaging methods are available for head-fixed larval  
69 zebrafish, imaging a speeding brain imposes many technical challenges. Current studies  
70 on freely swimming zebrafish are either limited to non-imaging optical systems [19] or  
71 wide field imaging at low resolution [20]. While light sheet microscopy (LSM) has  
72 demonstrated entire brain coverage and single neuron resolution in restrained zebrafish  
73 [12], it lacks the speed to follow rapid fish movement. Moreover, in LSM, the sample is  
74 illuminated from its side, a configuration that is difficult to be integrated with a tracking  
75 system. Conventional light field microscopy (LFM) [21, 22] is a promising alternative  
76 due to its higher imaging speed; however, its spatial resolution is relatively low.  
77 Specialized LFMs for monitoring neural activity utilizing temporal information were also  
78 developed recently [23, 24], which rely on spatiotemporal sparsity of fluorescent signals  
79 and cannot be applied to moving animals.

80

81 Here, we describe a fast 3D tracking technique and a novel volume imaging method that  
82 allow whole brain calcium imaging with high spatial and temporal resolution in freely  
83 behaving larval zebrafish. Zebrafish larvae possess extraordinary mobility. They can  
84 move at an instantaneous velocity up to 50 mm/s [25] and acceleration of 1 g ( $9.83 \text{ m/s}^2$ ).  
85 To continuously track fish motion, we developed a high-speed closed-loop system in  
86 which (1) customized machine vision software allowed rapid estimation of fish  
87 movement in both the x-y and z directions; and, (2) feedback control signals drove a

88 high-speed motorized x-y stage (at 300 Hz) and a piezo Z stage (at 100 Hz) to retain the  
89 entire fish head within the field of view of a high numerical aperture (25 $\times$ , NA = 1.05)  
90 objective.

91

92 Larval zebrafish can make sudden and swift movements that easily cause motion blur and  
93 severely degrade imaging quality. To overcome this obstacle, we developed a new  
94 eXtended field of view LFM (XLFM). The XLFM can image sparse neural activity over  
95 the larval zebrafish brain at near single cell resolution and at a volume rate of 77 Hz, with  
96 the aid of genetically encoded calcium indicator GCamp6f. Furthermore, the  
97 implementation of flashed fluorescence excitation (200  $\mu$ s in duration) allowed blur-free  
98 fluorescent images to be captured when a zebrafish moved at a speed up to 10 mm/s. The  
99 seamless integration of the tracking and imaging system made it possible to reveal rich  
100 whole brain neural dynamics during natural behavior with unprecedented resolution. We  
101 demonstrated the ability of our system during visually evoked and prey capture behaviors  
102 in larval zebrafish.

103

## 104 **Results:**

105 The newly developed XLFM is based on the general principle of light field [26] and can  
106 acquire 3D information from a single camera frame. XLFM greatly relaxed the constraint  
107 imposed by the tradeoff between spatial resolution and imaging volume coverage in  
108 conventional LFM. This achievement relies on optics and in computational  
109 reconstruction techniques. First, a customized lenslet array (Figure 1a, Figure 1-figure  
110 supplement 1) was placed at the rear pupil plane of the imaging objective, instead of at

111 the imaging plane as in LFM. Therefore, in ideal conditions, a spatially invariant point  
112 spread function (PSF) could be defined and measured. In practice, the PSF was  
113 approximately spatially invariant, as discussed below. Second, the aperture size of each  
114 micro-lens was decoupled from their interspacing and spatial arrangement, so that both  
115 the imaging volume and the resolution could be optimized simultaneously given the  
116 limited imaging sensor size. Third, multifocal imaging [27, 28] was introduced to further  
117 increase the depth of view by dividing the micro-lenses array into several groups whose  
118 focal planes were at different axial positions (Figures 1b & c, Figure 1-figure  
119 supplements 3 & 4). Fourth, a new computational algorithm based on optical wave theory  
120 was developed to reconstruct the entire 3D volume from one image (Figure 1-figure  
121 supplement 5) captured by a fast camera (see Methods).

122

123 We characterized the XLFM by imaging 0.5  $\mu\text{m}$  diameter fluorescent beads. In our  
124 design, the system had  $\sim \text{Ø}800 \mu\text{m}$  in plane coverage ( $\text{Ø}$  is the diameter of the lateral  
125 field of view) and more than 400  $\mu\text{m}$  depth of view, within which an optimal resolution  
126 of  $3.4 \mu\text{m} \times 3.4 \mu\text{m} \times 5 \mu\text{m}$  could be achieved over a depth of 200  $\mu\text{m}$  (Figure 1-figure  
127 supplements 6 & 7, Methods) when sample was sparse. In the current implementation,  
128 however, the imaging performance suffered from variation in the focal length of the  
129 micro-lenses (Figure 1-figure supplement 8) and the optimal resolution at  $3.4 \mu\text{m} \times 3.4$   
130  $\mu\text{m} \times 5 \mu\text{m}$  was preserved over a reduced volume of  $\text{Ø}500 \mu\text{m} \times 100 \mu\text{m}$  (Figure 1-figure  
131 supplements 9 & 10). Beyond this volume, the resolution degraded gradually. To  
132 minimize the reconstruction time while assuring whole brain coverage ( $\sim 250 \mu\text{m}$  thick),  
133 all imaging reconstructions were carried out over a volume of  $\text{Ø}800 \mu\text{m} \times 400 \mu\text{m}$ .

134

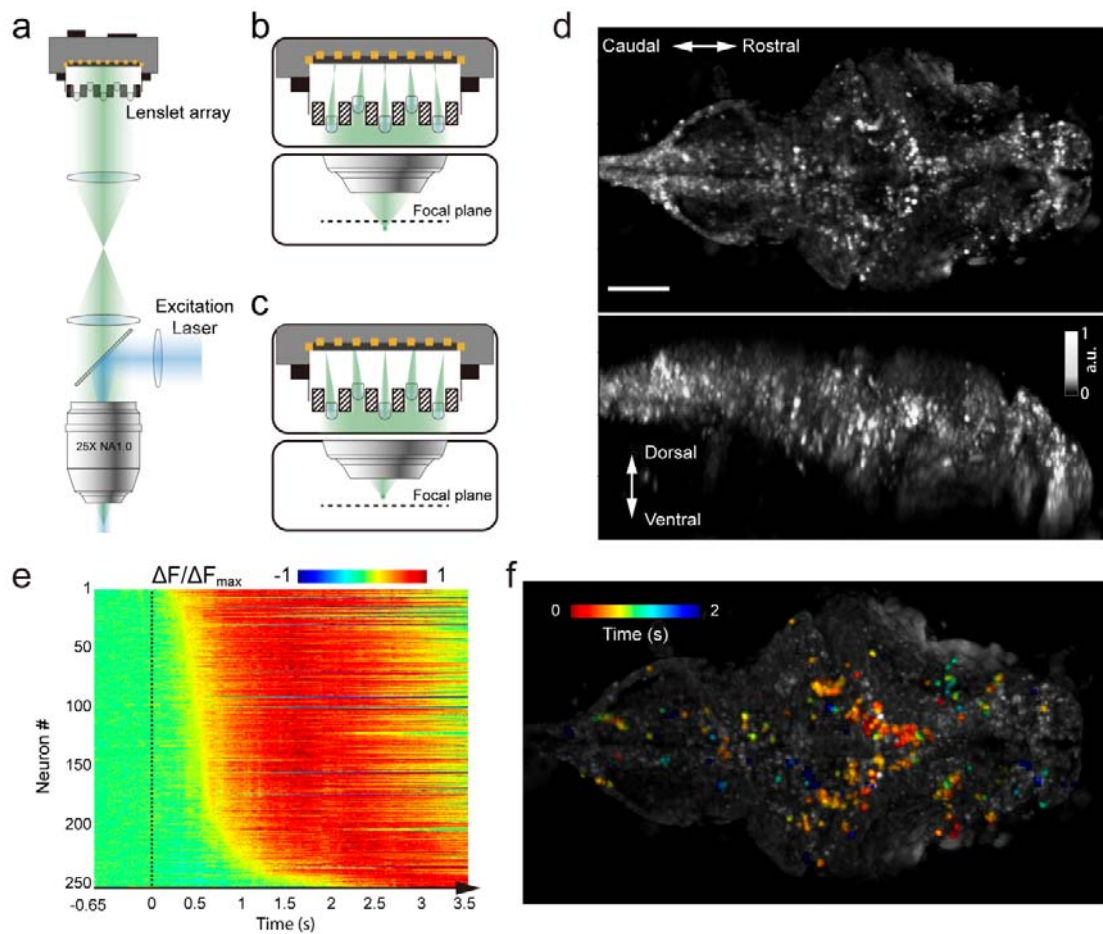
135 The achievable optimal resolution also relies on the sparseness of the sample, because the  
136 information captured by the image sensor was insufficient to assign independent values  
137 for all voxels in the entire reconstructed imaging volume. Given the total number of  
138 neurons ( $\sim 80,000$  [29]) in a larval zebrafish brain, we next introduced a sparseness index  
139  $\rho$ , defined as the fraction of neurons in the brain active at a given instant, and used  
140 numerical simulation to characterize the dependence of achievable resolution on  $\rho$ . We  
141 identified a critical  $\rho_c \approx 0.11$ , below which active neurons could be resolved at the  
142 optimal resolution (Figure 1-figure supplement 11b). As  $\rho$  increased, closely clustered  
143 neurons could no longer be well resolved (Figure 1-figure supplements 11c-d). Therefore,  
144 sparse neural activity is a prerequisite in XLFM for resolving individual neurons at the  
145 optimal resolution. Moreover, the above characterization assumed an aberration and  
146 scattering free environment; complex optical properties of biological tissue could also  
147 degrade the resolution [30].

148

149 We demonstrated the capabilities of XLFM by imaging the whole brain neuronal  
150 activities of a larval zebrafish (5 d post-fertilization (dpf)) at a speed of 77 volumes/s and  
151 relatively low excitation laser exposure of  $2.5 \text{ mW/mm}^2$  (Figure 1d, Video 1). The  
152 fluorescent intensity loss due to photobleaching reached  $\sim 50\%$  when the zebrafish,  
153 which expressed pan-neuronal nucleus-labelled GCamp6f (huc:h2b-gcamp6f), was  
154 imaged continuously for  $\sim 100$  min and over more than 300,000 volumes (Figure 1-figure  
155 supplement 12, Videos 2 & 3). To test whether XLFM could monitor fast changes in  
156 neuronal dynamics across the whole brain at high resolution (close to single neuron

157 level), we first presented the larval zebrafish, restrained in low melting point agarose,  
158 with visual stimulation (~ 2.6 s duration). We found that different groups of neurons in  
159 the forebrain, midbrain, and hindbrain were activated at different times (Figures 1e–f,  
160 Videos 1 & 4), suggesting rapid sensorimotor transformation across different brain  
161 regions.



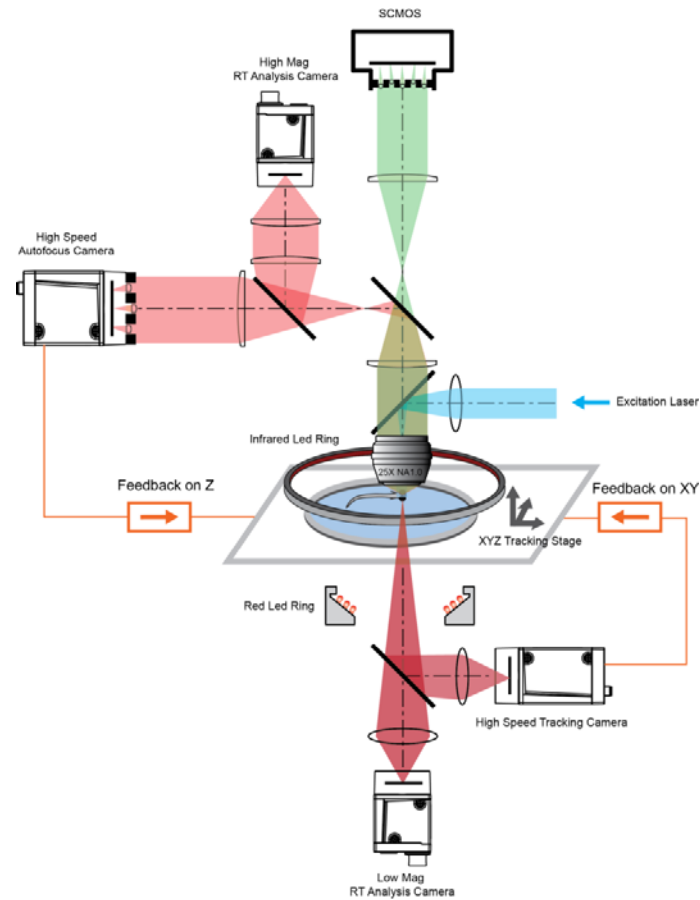


162

163 Figure 1. Whole brain imaging of larval zebrafish with XLFM. (a) Schematic of XLFM.  
164 Lenslet array position was conjugated to the rear pupil plane of the imaging objective.  
165 Excitation laser (blue) provided uniform illumination across the sample. (b–c) Point  
166 sources at two different depths formed, through two different groups of micro-lenses,  
167 sharp images on the imaging sensor, with positional information reconstructed from these  
168 distinct patterns. (d) Maximum intensity projections (MIPs) on time and space of time  
169 series volume images of an agarose-restrained larval zebrafish with pan-neuronal  
170 nucleus-localized GCaMP6f (*huc:h2b-gcamp6f*) fluorescence labeling. (e) Normalized  
171 neuronal activities of selected neurons exhibited increasing calcium responses after the  
172 onset of light stimulation at  $t = 0$ . Neurons were ordered by the onset time when the  
173 measured fluorescence signals reached 20% of their maximum. (f) Selected neurons in (e)  
174 were color coded based on their response onset time. Scale bar is 100  $\mu\text{m}$ .

175 To track freely swimming larval zebrafish, we transferred fish into a water-filled chamber  
176 with a glass ceiling and floor. The 20 mm × 20 mm × 0.8 mm-sized chamber was coupled  
177 with a piezo actuator and mounted on a high-speed 2D motorized stage (Figure 2). A  
178 tracking camera monitored the lateral movement of the fish, and an autofocus camera,  
179 which captured light field images, monitored the axial movement of the fish head (Figure  
180 2, Figure 2-figure supplement 1).

181



182

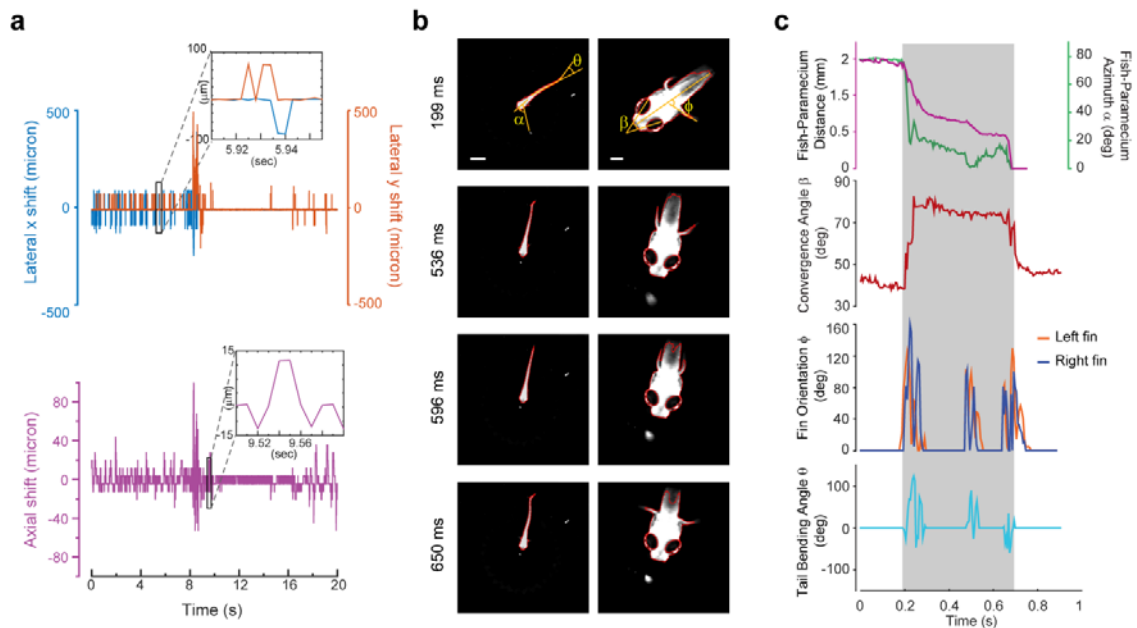
183 Figure 2. System schematics that integrated tracking, whole brain functional imaging, and  
184 real time behavioral analysis. Larval zebrafish swam in a customized chamber with an  
185 optically transparent ceiling and floor. The water-filled chamber was mounted on a high-  
186 speed three-axis stage (PI M686 & PI P725KHDS). Customized LED rings generated  
187 dark field illumination of the zebrafish. The scattered light was collected by four cameras:  
188 two cameras below the chamber were used for x-y plane tracking and low magnification  
189 real-time (RT) analysis, respectively; two cameras above the chamber and after the  
190 imaging objective were used for Z autofocus and high magnification RT analysis. The  
191 positional information of the larval zebrafish, acquired from the tracking and autofocus  
192 system, was converted to feedback voltage signals to drive the three-axis stage and to  
193 compensate for fish movement. The functional imaging system, described in Figure 1,  
194 shared the same imaging objective placed above the swimming chamber. The 3D  
195 tracking, RT behavioral analysis, and functional imaging system were synchronized for  
196 accurate correlation between neural activity and behavioral output.

197 Real-time machine vision algorithms allowed quick estimate of lateral (within 1 ms) and  
198 axial (~ 5 ms) head positions (see Methods). The error signals in three dimensions,  
199 defined as the difference between the head position and set point, were calculated (Figure  
200 3a) and converted to analog voltage signals through proportional-integral-derivative (PID)  
201 control to drive the motorized stage and z-piezo scanner. Tracking and autofocusing  
202 allowed for rapid compensation of 3D fish movement (300 Hz in x and y, 100 Hz in z,  
203 Figure 3a) and retainment of the fish head within the field of view of the imaging  
204 objective.

205

206 Our tracking system permitted high-speed and high-resolution recording of larval  
207 zebrafish behaviors. With two cameras acquiring head and whole body videos  
208 simultaneously (Figure 2, Figure 3b), we recorded and analyzed in real time (see  
209 Methods) the kinematics of key features during larval zebrafish prey capture (Figures 3b  
210 & c, Videos 5 & 6). Consistent with several earlier findings [16-18], eyes converged  
211 rapidly when the fish entered the prey capture state (Figure 3c). Other features that  
212 characterized tail and fin movement were also analyzed at high temporal resolution  
213 (Figure 3c).

214



215

216 Figure 3. 3D tracking of larval zebrafish. (a) Representative time varying error signals in  
217 three dimensions, defined as the difference between real head position and set point. Inset  
218 provides magnified view at short time interval. Lateral movement can be rapidly  
219 compensated for within a few milliseconds with an instantaneous velocity of up to 10  
220 mm/s. The axial shift was small compared with the depth coverage (200  $\mu\text{m}$ ) during  
221 whole brain imaging, and thereby had minor effect on brain activity reconstruction. (b)  
222 Tracking images at four time points during prey capture behavior, acquired at low (left)  
223 and high (right) magnification simultaneously. Scale bars are 1 mm (left) and 200  $\mu\text{m}$   
224 (right). (c) Kinematics of behavioral features during prey capture. Shaded region marks  
225 the beginning and end of the prey capture process.

226 The integration of the XLFM and 3D tracking system allowed us to perform whole brain  
227 functional imaging of a freely behaving larval zebrafish (Figure 2). We first replicated the  
228 light-evoked experiment (similar to Figure 1), albeit in a freely behaving zebrafish with  
229 pan-neuronal cytoplasm-labeled GCaMP6s (huc:gcamp6s), which exhibited faster and  
230 more prominent calcium response (Video 7). Strong activities were observed in the  
231 neuropil of the optical tectum and the midbrain after stimulus onset. The fish tried to  
232 avoid strong light exposure and made quick tail movement at  $\sim 60$  Hz. Whole brain  
233 neural activity was monitored continuously during the light-evoked behavior, except for  
234 occasional blurred frames due to the limited speed and acceleration of the tracking stage.

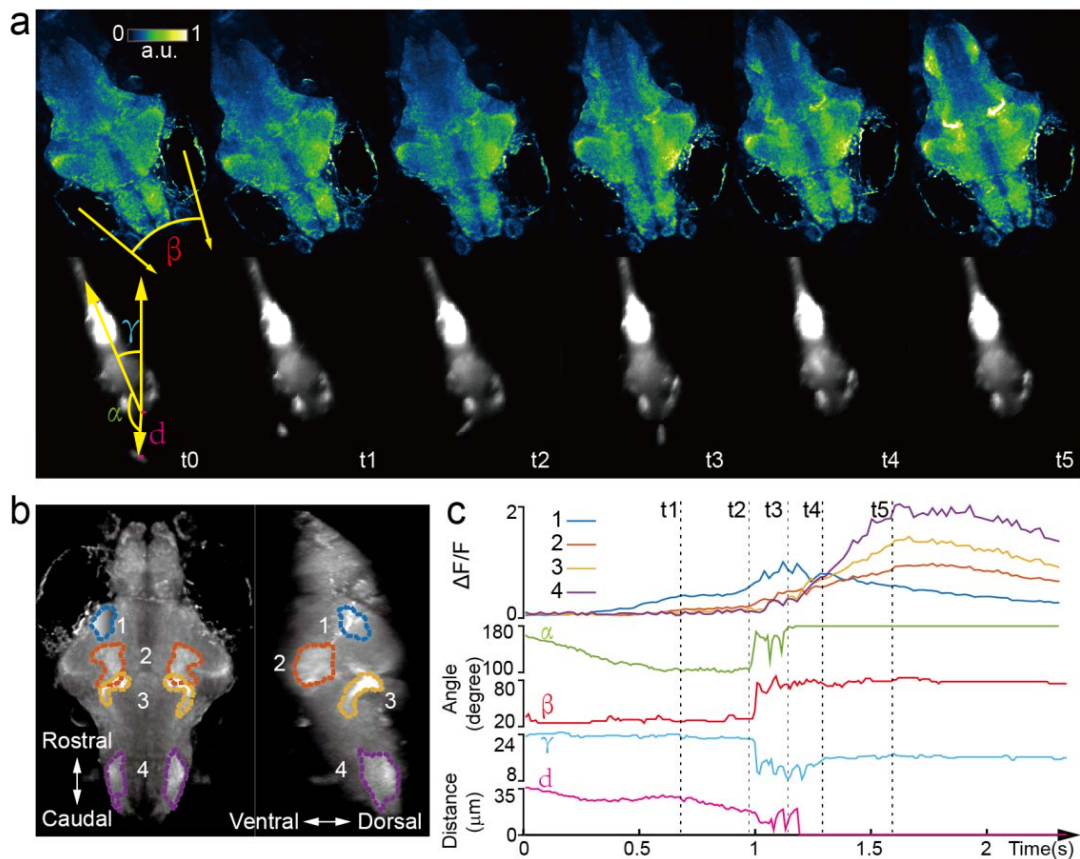
235

236 Next, we captured whole brain neural activity during the entire prey capture process in  
237 freely swimming larval zebrafish (huc:gcamp6s, Video 8). When a paramecium moved  
238 into the visual field of the fish, groups of neurons, indicated as group 1 in Figure 4b, near  
239 the contralateral optical tectum of the fish were first activated ( $t_1$ ). The fish then  
240 converged its eyes onto the paramecium and changed its heading direction in approach  
241 ( $t_2$ ). Starting from  $t_2$ , several groups of neurons in the hypothalamus, midbrain, and  
242 hindbrain, highlighted as groups 2, 3, and 4 in Figure 4b, were activated. It took the fish  
243 three attempts (Figure 4c) to catch and eat the paramecium. After the last try ( $t_4$ ), neuron  
244 activity in group 1 decreased gradually, whereas activities in the other groups of neurons  
245 continued to rise and persisted for  $\sim 1$  s before the calcium signals decreased. The earliest  
246 tectal activity (group 1) responsible for prey detection found here is consistent with  
247 previous studies [31, 32]. Moreover, our data revealed interesting neural dynamics arising  
248 from other brain regions during and after successful prey capture. We also monitored

249 similar behavior in a zebrafish expressing nucleus-localized GCamp6f (huc:h2b-gcamp6f)

250 with better resolution but less prominent calcium response (Video 9).

251



252

253 Figure 4. Whole brain imaging of larval zebrafish during prey capture behavior. (a)  
 254 Renderings of whole brain calcium activity at six time points (up) and the corresponding  
 255 behavioral images (bottom). Features used to quantify behavior were: fish-paramaecium  
 256 azimuth  $\alpha$ ; convergence angle between eyes  $\beta$ ; head orientation  $\gamma$ ; and fish-paramaecium  
 257 distance  $d$ . (b) Maximum intensity projections of zebrafish brain with pan-neuronal  
 258 cytoplasm-labeled GCaMP6s (huc:gcaMP6s). Boundaries of four brain regions are color  
 259 marked. (c) Neural dynamics inferred from GCaMP6 fluorescence changes in these four  
 260 regions during the entire prey capture behavior (up) and the kinematics of behavioral  
 261 features (bottom). Note that between t2 and t4, fish-paramaecium distance  $d$  exhibits three  
 262 abrupt kinks, representing the three attempts to catch prey.



263 **Discussion:**

264 Whole brain imaging in freely behaving animals has been previously reported in  
265 *Caenorhabditis elegans*, by integrating spinning-disk confocal microscopy with a 2D  
266 tracking system [33, 34]. In the more remote past, Howard Berg pioneered the use of 3D  
267 tracking microscopy to study bacteria chemotaxis [35]. However, the significant increase  
268 of animal size imposes challenges both in tracking and imaging technologies. The XLFM,  
269 derived from the general concept of light field imaging [21, 26, 36, 37], overcomes  
270 several critical limitations of conventional LFM and allows optimization of imaging  
271 volume, resolution, and speed simultaneously. Furthermore, it can be perfectly combined  
272 with flashed fluorescence excitation to capture blur-free images at high resolution during  
273 rapid fish movement. Taken together, we have developed a volume imaging and tracking  
274 microscopy system suitable for observing and capturing freely behaving larval zebrafish,  
275 which have ~ 80,000 neurons and can move two orders of magnitude faster than *C.*  
276 *elegans*.

277

278 Tracking and whole brain imaging of naturally behaving zebrafish provide an additional  
279 way to study sensorimotor transformation across the brain circuit. A large body of  
280 research suggests that sensory information processing depends strongly on the locomotor  
281 state of an animal [38-40]. The ability to sense self-motion, such as proprioceptive  
282 feedback [41] and efferent copy [42], can also profoundly shape the dynamics of the  
283 neural circuit and perception. To explore brain activity in swimming zebrafish, several  
284 studies have utilized an elegant tail-free embedding preparation [25, 43, 44], in which  
285 only the head of the fish is restrained in agarose for functional imaging. Nevertheless, it

286 would be ideal to have physiological access to all neurons in defined behavioral states,  
287 where all sensory feedback loops remain intact and functional. Our XLFM-3D tracking  
288 system is one step towards this goal, and could be better exploited to explore the neural  
289 basis of more sophisticated natural behaviors, such as prey capture and social interaction,  
290 where the integration of multiple sensory feedbacks becomes critical.

291

292 In the XLFM, the camera sensor size limited the number of voxels and hence the number  
293 of neurons that could be reliably reconstructed. Our simulation suggested that the  
294 sparseness of neuronal activities is critical for optimal imaging volume reconstruction. A  
295 growing body of experimental data indeed suggests that population neuronal activities are  
296 sparse [45, 46] and sparse representation is useful for efficient neural computation [47,  
297 48]. Given the total number of neurons in the larval zebrafish brain, we found that when  
298 the fraction of active neurons in a given imaging frame was less than  $\rho_c \approx 0.11$ , individual  
299 neurons could be resolved at optimal resolution. When population neural activity was  
300 dense (*e.g.*, neurons have high firing rate and firing patterns have large spatiotemporal  
301 correlation), we obtained a coarse-grained neural activity map with reduced resolution.

302

303 To retain the fish head within the field of view of the imaging objective, our tracking  
304 system compensated for fish movement by continuously adjusting the lateral positions of  
305 the motorized stage. As a result, self-motion perceived by the fish was not exactly the  
306 same as that during natural behaviors. The linear acceleration of the swimming fish,  
307 encoded by vestibular feedback, was significantly underestimated. The perception of  
308 angular acceleration during head orientation remained largely intact. The relative flow

309 velocity along the fish body, which was invariant upon stage translation, can still be  
310 detected by specific hair cells in the lateral line system [49, 50]. Together, the  
311 interpretation of brain activity associated with self-motion must consider motion  
312 compensation driven by the tracking system.

313

314 Both tracking and imaging techniques can be improved in the future. For example, the  
315 current axial displacement employed by the piezo scanner had a limited travelling range  
316 (400  $\mu\text{m}$ ), and our swimming chamber essentially restrained the movement of the  
317 zebrafish in two dimensions. This limitation could be relaxed by employing axial  
318 translation with larger travelling range and faster dynamics. Furthermore, to avoid any  
319 potential disturbance of animal behaviors, it would be ideal if the imaging system moved,  
320 instead of the swimming chamber.

321

322 In XLFM, the performance degradation caused by focal length variation of the micro-  
323 lenses could be resolved by higher precision machining. In addition, the capability of  
324 XLFM could be further improved with the aid of technology development in other areas.  
325 With more pixels in the imaging sensor, we could resolve more densely labelled samples,  
326 and achieve higher spatial resolution without sacrificing imaging volume coverage by  
327 introducing more than two different focal planes formed by more groups of micro-lenses.  
328 With better imaging objectives that could provide higher numerical aperture and larger  
329 field of view at the same time, we could potentially image the entire nervous system of  
330 the larval zebrafish with single neuron resolution in all three dimensions. Additionally,  
331 the fast imaging speed of XLFM holds the potential for recording electrical activity when

332 high signal-to-noise ratio (SNR) fluorescent voltage sensors become available [51].  
333 Finally, the illumination-independent characteristic of XLFM is perfectly suitable for  
334 recording brain activities from bioluminescent calcium/voltage indicators in a truly  
335 natural environment, where light interference arising from fluorescence excitation can be  
336 eliminated [19].

337

## 338 **METHODS**

### 339 **XLFM**

340 The imaging system (Figure 1) was a customized upright microscope. Along the  
341 fluorescence excitation light path, a blue laser (Coherent, OBIS 488 nm, 100 mW, USA)  
342 was expanded and collimated into a beam with a diameter of  $\sim 25$  mm. It was then  
343 focused by an achromatic lens (focal length: 125 mm) and reflected by a dichroic mirror  
344 (Semrock, Di02-R488-25x36, USA) into the back pupil of the imaging objective  
345 (Olympus, XLPLN25XWMP2, 25X, NA 1.05, WD 2mm, Japan) to result in an  
346 illumination area of  $\sim 1.44$  mm in diameter near the objective's focal plane. In the  
347 fluorescence imaging light path, excited fluorescence was collected by the imaging  
348 objective and transmitted through the dichroic mirror. A pair of achromatic lenses (focal  
349 lengths:  $F_1 = 180$  mm &  $F_2 = 160$  mm), arranged in  $2F_1 + 2F_2$ , were placed after the  
350 objective and dichroic mirror to conjugate the objective's back pupil onto a customized  
351 lenslet array (Figure 1-figure supplement 1). The customized lenslet array was an  
352 aluminum plate with 27 holes (1.3 mm diameter aperture on one side and 1 mm diameter  
353 aperture on the other side, Source Code File 1) housing 27 customized micro-lenses (1.3  
354 mm diameter, focal length: 26 mm). The 27 micro-lenses were divided into two groups  
355 (Figure 1-figure supplement 1) and an axial displacement of 2.5 mm was introduced  
356 between them. Due to the blockage of light by the aluminum micro-lenses housing, 16%  
357 of the light after a 1.05 NA imaging objective was effectively collected by the camera.  
358 This efficiency is equivalent to using a 0.4 NA imaging objective. Finally, the imaging  
359 sensor of a sCMOS camera (Hamamatsu, Orca-Flash 4.0 v2, Japan) was placed at the  
360 middle plane between two focal planes formed by two different groups of micro-lenses.

361 The total magnification of the imaging system was  $\sim 4$ , so one camera pixel ( $6.5 \mu\text{m}$ )  
362 corresponded to  $\sim 1.6 \mu\text{m}$  on the sample.

363

364 We developed a computational algorithm for 3D volume reconstruction, which required  
365 an accurately measured PSF (Figure 1-figure supplement 2). The PSF was measured by  
366 recording images of a 500 nm diameter fluorescent bead sitting on a motorized stage  
367 under the objective. A stack of 200 images was recorded when the bead was scanned with  
368 a step size of  $2 \mu\text{m}$  in the axial direction from  $200 \mu\text{m}$  below the objective's focal plane  
369 to  $200 \mu\text{m}$  above. Since the images formed by two different groups of micro-lenses were  
370 from different axial locations and had different magnifications, the measured raw PSF  
371 data were reorganized into two complementary parts: PSF\_A and PSF\_B (Figure 1-figure  
372 supplements 3 & 4), according to the spatial arrangement of the micro-lenses. We took  
373 PSF\_A stack, PSF\_B stack, and a single frame of a raw image ( $2048 \times 2048$  pixels) as  
374 inputs, and applied a newly developed algorithm to reconstruct the 3D volume.

375

### 376 **Image reconstruction of XLFM**

377 The reconstruction algorithm was derived from the Richardson-Lucy deconvolution. The  
378 goal was to reconstruct a 3D fluorescent object from a 2D image:

$$Obj(x, y, z)$$

379 The algorithm assumes that the real 3D object can be approximated by a discrete number  
380 of x-y planes at different  $z$  positions:

$$381 \quad Obj(x, y, z) \sim Obj(x, y, z_k), \text{ where } k = 1, 2 \dots n$$

382 The numbers and positions of these planes can be arbitrary, yet the Nyquist sampling rate  
383 should be chosen to optimize the speed and accuracy of the reconstruction.

384 As the imaging system consisted of two different groups of micro-lenses (Figure 1-figure  
385 supplement 1), their PSFs (Figure 1-figure supplements 3 & 4) each consisted of a stack  
386 of planes that were measured at the same chosen axial positions  $z_k$ :

$$387 \quad PSF_A(x, y, z_k) \text{ \& } PSF_B(x, y, z_k),$$

388 Although the PSF was measured in imaging space, here we denote  $x$  and  $y$  as coordinates  
389 in object space to follow conventions in optical microscopy. Here and below, the  
390 combination of  $PSF_A$  and  $PSF_B$  is the total PSF.

391

392 Additionally, the images formed by two different groups of micro-lenses had different  
393 magnifications, which could be determined experimentally. The ratio between two  
394 different magnifications can be defined as:

$$\gamma = \frac{\text{Magnification of group A microlenses}}{\text{Magnification of group B microlenses}}$$

395 Then the captured image on the camera can be estimated as:

$$Img_{Est}(x, y) = \sum_{k=1}^n \{Obj_A(x, y, z_k) \otimes PSF_A(x, y, z_k) + Obj_B(x, y, z_k) \otimes PSF_B(x, y, z_k)\},$$

$$396 \quad \text{where } Obj_A(x, y, z_k) = Obj_B(\gamma x, \gamma y, z_k)$$

397 The operator  $\otimes$  represents 2D convolution. Here,  $x$  and  $y$  on the left hand side of the  
398 equation also represent coordinates in object space so that 2D convolution was carried  
399 out in the same coordinates.

400

401 The goal of the algorithm is to estimate the  $Obj(x, y, z_k)$  from the measured camera  
402 frame:

$$Img_{Meas}(x, y)$$

403 According to the Richardson-Lucy deconvolution algorithm, the iterative reconstruction  
 404 can be expressed as:

$$Img_{Est}^i(x, y) = \sum_{k=1}^n \{Obj_A^{i-1}(x, y, z_k) \otimes PSF_A(x, y, z_k) + Obj_B^{i-1}(x, y, z_k) \otimes PSF_B(x, y, z_k)\}$$

$$Obj_A^{tmp}(x, y, z_k) = Obj_A^{i-1}(x, y, z_k) \left\{ \frac{Img_{Meas}(x, y)}{Img_{Est}^i(x, y)} \otimes PSF_A(-x, -y, z_k) \right\}$$

$$Obj_B^{tmp}(x, y, z_k) = Obj_B^{i-1}(x, y, z_k) \left\{ \frac{Img_{Meas}(x, y)}{Img_{Est}^i(x, y)} \otimes PSF_B(-x, -y, z_k) \right\}$$

$$Obj_A^i(x, y, z_k) = w(z_k) Obj_A^{tmp}(x, y, z_k) + (1 - w(z_k)) Obj_B^{tmp}(x, y, z_k)$$

$$Obj_B^i(x, y, z_k) = w(z_k) Obj_A^{tmp}\left(\frac{x}{\gamma}, \frac{y}{\gamma}, z_k\right) + (1 - w(z_k)) Obj_B^{tmp}(x, y, z_k)$$

405 Here  $0 \leq w(z_k) \leq 1$  is the weighting factor at different axial positions. The choice of  
 406  $w(z_k)$  can be arbitrary. Because the resolutions achieved by different groups of micro-  
 407 lenses at different  $z$  positions were not the same, the weighting factor can take this effect  
 408 into consideration by weighing higher quality information more than lower quality  
 409 information. One simple choice is  $w(z_k) = 0.5$ , that is, to weigh information from two  
 410 groups of micro-lenses equally.

411

412 The starting estimate of the object can be any non-zero value. Near the end of the  
 413 iterations,  $Obj_A^i(x, y, z_k)$  and  $Obj_B^i(x, y, z_k)$  are interchangeable, except with different  
 414 magnifications. Either can be used as the resulting estimate of the 3D object.

415

416 In XLFM, together with its reconstruction algorithm, the diffraction of the 3D light field  
 417 is properly considered by experimentally measured PSF. The raw imaging data can be fed  
 418 into the algorithm directly without any preprocessing. Given that the PSF is spatially



419 invariant, which is satisfied apart from small aberrations, the algorithm can handle  
420 overlapping fish images (Figure 1-figure supplement 5). As a result, the field of view can  
421 be increased significantly. The reconstruction algorithm was typically terminated after 30  
422 iterations when modifications in the estimated object became very small. The  
423 computation can speed up significantly via GPU. It took about 4 min to reconstruct one  
424 3D volume using a desktop computer with a GPU (Nvidia Titan X). In comparison, the  
425 reconstruction ran  $\sim 20\times$  slower using a CPU (Intel E5-2630v2) on a Dell desktop. The  
426 source code written in MATLAB can be found in the Source Code File 2.

427

428 The 3D deconvolution method has been developed for conventional LFM [21]. Our  
429 method differs from [21] in several ways. (1) The optical imaging systems are different.  
430 (2) The definitions of PSFs are different. Ours defines a spatially *invariant* PSF (see  
431 below for detailed characterization), whereas [21] defined a spatially variant PSF, leading  
432 to increased computational complexity in the deconvolution algorithm. (3) The PSF in  
433 [21] was simulated based on a model derived from an ideal imaging system, whereas ours  
434 was measured experimentally. Furthermore, our system took practical conditions, such as  
435 a non-ideal imaging objective, actual positions of microlenses, the spectrum of received  
436 fluorescence signal *et al.*, into consideration.

437

#### 438 **Resolution characterization of XLFM**

439 Unlike conventional microscopy, where the performance of the imaging system is fully  
440 characterized by the PSF at the focal plane, the capability of XLFM is better  
441 characterized as a function of positions throughout the imaging volume.

442

443 We first characterized the spatial resolution in the x-y plane by analyzing the spatial  
444 frequency support of the experimentally measured PSF from individual micro-lenses  
445 using a 0.5  $\mu\text{m}$  diameter fluorescent bead. The optical transfer function (OTF), which is  
446 the Fourier transform of the PSF in the x-y plane, was extended to a spatial frequency of  
447  $\sim 1/3.4 \mu\text{m}^{-1}$  (Figure 1-figure supplement 6), a result that agreed well with the designed  
448 resolution at 3.4  $\mu\text{m}$ , given that the equivalent NA of individual micro-lenses was 0.075.

449

450 The lateral resolution, measured from the raw PSF behind individual micro-lenses, was  
451 preserved across the designed cylindrical imaging volume of  $\text{Ø}800 \mu\text{m} \times 200 \mu\text{m}$  (Figure  
452 1-figure supplement 6). However, the reconstruction results (Figure 1-figure supplement  
453 9), which used total PSF (Figure 1-figure supplement 2), exhibited resolution degradation  
454 when the fluorescent bead was placed more than 250  $\mu\text{m}$  away from the center (Figure 1-  
455 figure supplement 9). This discrepancy resulted from the variation in focal length of the  
456 micro-lenses (Figure 1-figure supplement 8), which, in turn, led to spatial variance of the  
457 defined  $PSF_A$  and  $PSF_B$ . In principle, the designed lateral resolution of 3.4  $\mu\text{m}$  could be  
458 preserved over a volume of  $\text{Ø}800 \mu\text{m} \times 200 \mu\text{m}$  by reducing focal length variation to  
459 below 0.3%

460

461 We next characterized the axial resolution of the XLFM. The XLFM gained axial  
462 resolution by viewing the object from large projection angles achieved by micro-lenses  
463 sitting near the edge of the objective's back pupil plane. For example, if two points of  
464 light source were located at the same position in the X-Y plane, but were separated by  $\Delta z$

465 in the axial direction, then one micro-lens in the XLFM could capture an image of these  
466 two points with a shift between them. The shift can be determined as:

467 
$$d = \Delta z * \tan\theta,$$

468 where  $\theta$  is the inclination angle inferred from the measured PSF (Figure 1-figure  
469 supplement 2). If the two points in the image can be resolved, the two points separated by  
470  $\Delta z$  can be resolved by the imaging system. Since a micro-lens sitting in the outer layer of  
471 the array offered the largest inclination angle of 40 degree in our system, the axial  
472 resolution  $dz$  can be directly calculated as:

$$dz = \frac{dxy}{\tan\theta_{max}} = \frac{3.4 \mu m}{\tan(40^\circ)} = 4 \mu m$$

473 The best way to confirm the theoretical estimate is to image two fluorescent beads with  
474 precisely controlled axial separations. However, this is technically very challenging.  
475 Instead, we pursued an alternative method that is equivalent to imaging two beads  
476 simultaneously:

- 477 (1) We took a z stack of images of fluorescent beads, as done in measuring the PSF.  
478 (2) In post processing, we added two images from different z positions to mimic the  
479 beads being present simultaneously at two different z positions.

480

481 The above method allowed us to experimentally characterize the axial resolution afforded  
482 by individual micro-lenses focusing at different z positions. We used a single fluorescent  
483 bead (0.5  $\mu m$  in diameter) with a high SNR (Figure 1-figure supplement 7a). We imaged  
484 at different axial positions:  $z = -100 \mu m$ ,  $z = 0 \mu m$ , and  $z = 100 \mu m$  (Figure 1-figure  
485 supplement 7b). The third column is the combined images in column 1 & 2. The  
486 capability of resolving the two beads in the third column can be demonstrated by spatial

487 frequency analysis (fourth column in Figure 1-figure supplement 7b). The two line dips,  
488 indicating the existence of two beads instead of one rod in the fourth column, were  
489 confirmations of the resolving capability. This becomes more evident after deconvolution  
490 of the raw images (fifth column in Figure 1-figure supplement 7b). Micro-lenses 1 and 2  
491 could resolve two beads, separated by  $5\mu\text{m}$ , within the range of  $-100\mu\text{m} \leq z \leq 0$  and  
492  $0 \leq z \leq 100\mu\text{m}$ , respectively. In other words, the complementary information provided  
493 by the two micro-lenses allowed the system to maintain a high axial resolution at  $5\mu\text{m}$   
494 across a  $200\mu\text{m}$  depth.

495

496 Next, we imaged densely packed fluorescent beads ( $0.5\mu\text{m}$  in diameter) with a low SNR  
497 (Figure 1-figure supplement 10a), and used our reconstruction algorithm to determine the  
498 minimum axial separation between beads that could be resolved (Figure 1-figure  
499 supplements 10b–c). In this case,  $5\mu\text{m}$  axial resolution could be preserved across a depth  
500 of  $100\mu\text{m}$ . The resolution decayed gradually to  $\sim 10\mu\text{m}$  at the edge of an imaging  
501 volume with a  $400\mu\text{m}$  axial coverage (Figure 1-figure supplement 10b). We believe that  
502 the optimal axial resolution at  $5\mu\text{m}$  could be achieved over an axial coverage of  $200\mu\text{m}$   
503 by minimizing micro-lens focal length variation (Figure 1-figure supplement 8).

504

505 Finally, we characterized how the imaging performance depended upon the sparseness of  
506 the sample. Given the total number of neurons ( $\sim 80,000$ ) in a larval zebrafish brain, we  
507 introduced a sparseness index  $\rho$ , defined as the fraction of neurons in the brain active at  
508 an imaging frame, and used numerical simulation to characterize the dependence of  
509 achievable resolution on  $\rho$ . To this end, we simulated a zebrafish larva with uniformly

510 distributed firing neurons (red dots in Figure 1-figure supplement 11a). By convolving  
511 the simulated zebrafish with the experimentally measured PSFs (Figure 1-figure  
512 supplements 3 & 4), we generated an image that mimicked the raw data captured by the  
513 camera. We then reconstructed the simulated neurons from this image, represented by  
514 green dots. When  $\rho$  was equal to or less than 0.11, which corresponded to  $\sim 9000$  neurons  
515 activated at a given instant, all active neurons, including those closely clustered, could be  
516 reconstructed with optimal resolution (Figure 1-figure supplement 11b inset). As the  
517 sparseness index  $\rho$  increased, the resolution degraded: nearby neurons merged laterally  
518 and elongated axially (Figure 1-figure supplements 11c–d). In all calculations, the  
519 Poisson noise was properly considered by assuming that each active neuron emitted  
520 20,000 photons, 2.2% of which were collected by our imaging system.

521

522 *In vivo* resolution characterization is challenging due to a lack of bright and spot-like  
523 features in living animals. Additionally, achievable resolution depends on the optical  
524 properties of biological tissues, which can be highly heterogeneous and difficult to infer.  
525 The light scattering and aberration induced by biological tissue usually leads to degraded  
526 imaging performance [30, 52-54].

527

### 528 **XY tracking system**

529 To compensate for lateral fish movement and retain the entire fish head within the field  
530 of view of a high NA objective (25 $\times$ , NA = 1.05), a high-speed camera was used to  
531 capture fish motion (2 ms exposure time, 300 fps or higher, Basler aca2000-340kmNIR,  
532 Germany). We developed an FPGA-based RT system in LabVIEW that could rapidly

533 identify the head position by processing the pixel stream data within the Cameralink card  
534 before the whole image was transferred to RAM. The error signal between the actual  
535 head position and the set point was then fed into the PID to generate output signals and  
536 control the movement of a high-speed motorized stage (PI M687 ultrasonic linear motor  
537 stage, Germany). In the case of large background noise, we alternatively performed  
538 conventional imaging processing in C/C++ (within 1 ms delay). The rate-limiting factor  
539 of our lateral tracking system was the response time of the stage (~ 300 Hz).

540

#### 541 **Autofocus system**

542 We applied the principle of LFM to determine the axial movement of larval zebrafish.  
543 The autofocus camera (100 fps, Basler aca2000-340kmNIR, Germany) behind a one-  
544 dimensional micro-lens array captured triplet images of the fish from different  
545 perspectives (Figure 2-figure supplement 1a). Z motion caused an extension or  
546 contraction between the centroids of the fish head in the left and right sub-images, an  
547 inter-fish distance (Figure 2-figure supplement 1b) that can be accurately computed from  
548 image autocorrelation. The inter-fish distance, multiplied by a pre-factor, can be used to  
549 estimate the z position of the fish, as it varies linearly with axial movement (Figure 2-  
550 figure supplement 1c). The error signal between the actual axial position of the fish head  
551 and the set point was then fed into the PID to generate an output signal to drive a piezo-  
552 coupled fish container. The feedback control system was written in LabVIEW. The code  
553 was further accelerated by parallel processing and the closed loop delay was ~ 5 ms. The  
554 rate-limiting factor of the autofocus system was the settling time of the piezo scanner (PI  
555 P725KHDS, Germany, 400  $\mu\text{m}$  travelling distance), which was about 10 ms.

556

557 **Real-time behavioral analysis**

558 Two high-speed cameras acquired dark-field images at high and low magnification,  
559 respectively, and customized machine vision software written in C/C++ with the aid of  
560 OpenCV library was used to perform real-time behavioral analysis of freely swimming  
561 larval zebrafish. At high magnification, eye positions, their orientation, and convergence  
562 angle were computed; at low magnification, the contour of the whole fish, centerline,  
563 body curvature, and bending angle of the tail were computed. The high mag RT analysis  
564 was run at ~ 120 fps and the low mag RT analysis was run at ~ 180 fps. The source code  
565 can be found in the Source Code File 3.

566

567 **Ethics statement and animal handling**

568 All animal handling and care were conducted in strict accordance with the guidelines and  
569 regulations set forth by the Institute of Neuroscience, Chinese Academy of Sciences,  
570 University of Science and Technology of China (USTC) Animal Resources Center, and  
571 University Animal Care and Use Committee. The protocol was approved by the  
572 Committee on the Ethics of Animal Experiments of the USTC (permit number:  
573 USTCACUC1103013).

574

575 All larval zebrafish (*huc:h2b-gcamp6f* and *huc:gcamp6s*) were raised in embryo medium  
576 under 28.5°C and a 14/10 h light/dark cycle. Zebrafish were fed with paramecium from 4  
577 dpf. For restrained experiments, 4–6 dpf zebrafish were embedded in 1% low melting  
578 point agarose. For freely moving experiments, 7–11 dpf zebrafish with 10% Hank's

579 solution were transferred to a customized chamber (20 mm in diameter, 0.8 mm in depth),  
580 and 10–20 paramecia were added before the chamber was covered by a coverslip.

581

### 582 **Neural activity analysis**

583 To extract neural activity induced by visual stimuli (Figures 1e & f), time series 3D  
584 volume stacks were first converted to a single 3D volume stack, in which each voxel  
585 represented variance of voxel values over time. Candidate neurons were next extracted by  
586 identifying local maxima in the converted 3D volume stack. The region-of-interest (ROI)  
587 was set according to the empirical size of a neuron. The voxels around the local maxima  
588 were selected to represent neurons. The fluorescence intensity over each neuron's ROI  
589 was integrated and extracted as neural activity. Relative fluorescent changes  $\Delta F/F_0$  were  
590 normalized to their maximum calcium response  $\Delta F_{max}/F_0$  over time, and sorted  
591 according to their onset time when  $\Delta F$  first reached 20% of its  $\Delta F_{max}$  (Figures 1e & f)  
592 after the visual stimulus was presented.

593

### 594 **Visual stimulation**

595 A short wavelength LED was optically filtered (short-pass optical filter with cut-off  
596 wavelength at 450 nm, Edmund #84-704) to avoid light interference with fluorescence. It  
597 was then focused by a lens into a spot 2~3 mm in diameter. The zebrafish was  
598 illuminated from its side. The total power of the beam was roughly 3 mW.

599

### 600 **Statement of replicates and repeats in experiments**



601 Each experiment was repeated at least three times with similar experimental conditions.  
602 Imaging and video data acquired from behaviorally active larval zebrafish with normal  
603 huc:h2b-gcamp6f or huc:gcamp6s expression were used in the main figures and videos.

604

## 605 **References:**

- 606 1. Kerr, J.N.D. and W. Denk, *Imaging in vivo: watching the brain in action*. Nature  
607 Reviews Neuroscience, 2008. **9**(3): p. 195-205.
- 608 2. Dombeck, D.A., et al., *Imaging large-scale neural activity with cellular  
609 resolution in awake, mobile mice*. Neuron, 2007. **56**(1): p. 43-57.
- 610 3. Wyart, C., et al., *Optogenetic dissection of a behavioural module in the  
611 vertebrate spinal cord*. Nature, 2009. **461**(7262): p. 407-U105.
- 612 4. Boyden, E.S., et al., *Millisecond-timescale, genetically targeted optical control  
613 of neural activity*. Nature Neuroscience, 2005. **8**(9): p. 1263-1268.
- 614 5. Zhang, F., et al., *Multimodal fast optical interrogation of neural circuitry*.  
615 Nature, 2007. **446**(7136): p. 633-U4.
- 616 6. Chen, T.W., et al., *Ultrasensitive fluorescent proteins for imaging neuronal  
617 activity*. Nature, 2013. **499**(7458): p. 295-+.
- 618 7. Tian, L., et al., *Imaging neural activity in worms, flies and mice with improved  
619 GCaMP calcium indicators*. Nature Methods, 2009. **6**(12): p. 875-U113.
- 620 8. Luo, L., E.M. Callaway, and K. Svoboda, *Genetic dissection of neural circuits*.  
621 Neuron, 2008. **57**(5): p. 634-660.
- 622 9. Friedrich, R.W., G.A. Jacobson, and P. Zhu, *Circuit neuroscience in zebrafish*.  
623 Curr Biol, 2010. **20**(8): p. R371-81.
- 624 10. Ahrens, M.B. and F. Engert, *Large-scale imaging in small brains*. Curr Opin  
625 Neurobiol, 2015. **32**: p. 78-86.
- 626 11. Ahrens, M.B., et al., *Brain-wide neuronal dynamics during motor adaptation in  
627 zebrafish*. Nature, 2012. **485**(7399): p. 471-7.
- 628 12. Ahrens, M.B., et al., *Whole-brain functional imaging at cellular resolution using  
629 light-sheet microscopy*. Nat Methods, 2013. **10**(5): p. 413-20.
- 630 13. Engert, F., *The big data problem: turning maps into knowledge*. Neuron, 2014.  
631 **83**(6): p. 1246-8.
- 632 14. Engert, F., *Fish in the matrix: motor learning in a virtual world*. Front Neural  
633 Circuits, 2012. **6**: p. 125.
- 634 15. Bianco, I.H., et al., *The tangential nucleus controls a gravito-inertial vestibulo-  
635 ocular reflex*. Curr Biol, 2012. **22**(14): p. 1285-95.
- 636 16. Bianco, I.H., A.R. Kampff, and F. Engert, *Prey capture behavior evoked by  
637 simple visual stimuli in larval zebrafish*. Front Syst Neurosci, 2011. **5**: p. 101.
- 638 17. Patterson, B.W., et al., *Visually guided gradation of prey capture movements in  
639 larval zebrafish*. J Exp Biol, 2013. **216**(Pt 16): p. 3071-83.

- 640 18. Trivedi, C.A. and J.H. Bollmann, *Visually driven chaining of elementary swim*  
641 *patterns into a goal-directed motor sequence: a virtual reality study of*  
642 *zebrafish prey capture*. *Front Neural Circuits*, 2013. **7**: p. 86.
- 643 19. Naumann, E.A., et al., *Monitoring neural activity with bioluminescence during*  
644 *natural behavior*. *Nat Neurosci*, 2010. **13**(4): p. 513-20.
- 645 20. Muto, A., et al., *Real-time visualization of neuronal activity during perception*.  
646 *Curr Biol*, 2013. **23**(4): p. 307-11.
- 647 21. Broxton, M., et al., *Wave optics theory and 3-D deconvolution for the light field*  
648 *microscope*. *Opt Express*, 2013. **21**(21): p. 25418-39.
- 649 22. Prevedel, R., et al., *Simultaneous whole-animal 3D imaging of neuronal activity*  
650 *using light-field microscopy*. *Nat Methods*, 2014. **11**(7): p. 727-30.
- 651 23. Pégard, N.C., et al., *Compressive light-field microscopy for 3D neural activity*  
652 *recording*. *Optica*, 2016. **3**(5): p. 517-524.
- 653 24. Nobauer, T., et al., *Video rate volumetric Ca<sup>2+</sup> imaging across cortex using*  
654 *seeded iterative demixing (SID) microscopy*. *Nat Meth*, 2017. **14**(8): p. 811-  
655 818.
- 656 25. Severi, K.E., et al., *Neural control and modulation of swimming speed in the*  
657 *larval zebrafish*. *Neuron*, 2014. **83**(3): p. 692-707.
- 658 26. Adelson, E.H. and J.Y.A. Wang, *Single Lens Stereo with a Plenoptic Camera*. *Ieee*  
659 *Transactions on Pattern Analysis and Machine Intelligence*, 1992. **14**(2): p.  
660 99-106.
- 661 27. Abrahamsson, S., et al., *Fast multicolor 3D imaging using aberration-corrected*  
662 *multifocus microscopy*. *Nat Meth*, 2013. **10**(1): p. 60-63.
- 663 28. Perwass, C. and L. Wietzke. *Single lens 3D-camera with extended depth-of-*  
664 *field*. 2012.
- 665 29. Hill, A., et al., *Neurodevelopmental defects in zebrafish (Danio rerio) at*  
666 *environmentally relevant dioxin (TCDD) concentrations*. *Toxicological*  
667 *Sciences*, 2003. **76**(2): p. 392-399.
- 668 30. Ji, N., *Adaptive optical fluorescence microscopy*. *Nat Meth*, 2017. **14**(4): p. 374-  
669 380.
- 670 31. Semmelhack, J.L., et al., *A dedicated visual pathway for prey detection in larval*  
671 *zebrafish*. *Elife*, 2014. **3**.
- 672 32. Bianco, I.H. and F. Engert, *Visuomotor transformations underlying hunting*  
673 *behavior in zebrafish*. *Curr Biol*, 2015. **25**(7): p. 831-46.
- 674 33. Venkatachalam, V., et al., *Pan-neuronal imaging in roaming Caenorhabditis*  
675 *elegans*. *Proc Natl Acad Sci U S A*, 2016. **113**(8): p. E1082-8.
- 676 34. Nguyen, J.P., et al., *Whole-brain calcium imaging with cellular resolution in*  
677 *freely behaving Caenorhabditis elegans*. *Proc Natl Acad Sci U S A*, 2016.  
678 **113**(8): p. E1074-81.
- 679 35. Berg, H.C., *How to Track Bacteria*. *Review of Scientific Instruments*, 1971.  
680 **42**(6): p. 868-&.
- 681 36. Ng, R., et al., *Light Field Photography with a Hand-held Plenoptic Camera*.  
682 *Stanford Tech Report* 2005.
- 683 37. Levoy, M., et al., *Light field microscopy*. *ACM Trans. on Graphics (Proc*  
684 *SIGGRAPH)*, 2006. **25**: p. 924-934.

- 685 38. Niell, C.M. and M.P. Stryker, *Modulation of visual responses by behavioral state*  
686 *in mouse visual cortex*. *Neuron*, 2010. **65**(4): p. 472-9.
- 687 39. Maimon, G., A.D. Straw, and M.H. Dickinson, *Active flight increases the gain of*  
688 *visual motion processing in Drosophila*. *Nat Neurosci*, 2010. **13**(3): p. 393-9.
- 689 40. Chiappe, M.E., et al., *Walking modulates speed sensitivity in Drosophila motion*  
690 *vision*. *Curr Biol*, 2010. **20**(16): p. 1470-5.
- 691 41. Pearson, K.G., *Proprioceptive regulation of locomotion*. *Current Opinion in*  
692 *Neurobiology*, 1995. **5**(6): p. 786-791.
- 693 42. Bell, C.C., *An Efference Copy Which Is Modified by Reafferent Input*. *Science*,  
694 1981. **214**(4519): p. 450-453.
- 695 43. Portugues, R. and F. Engert, *Adaptive locomotor behavior in larval zebrafish*.  
696 *Front Syst Neurosci*, 2011. **5**: p. 72.
- 697 44. Portugues, R., et al., *Whole-brain activity maps reveal stereotyped, distributed*  
698 *networks for visuomotor behavior*. *Neuron*, 2014. **81**(6): p. 1328-43.
- 699 45. Hromadka, T., M.R. Deweese, and A.M. Zador, *Sparse representation of sounds*  
700 *in the unanesthetized auditory cortex*. *PLoS Biol*, 2008. **6**(1): p. e16.
- 701 46. Buzsaki, G. and K. Mizuseki, *The log-dynamic brain: how skewed distributions*  
702 *affect network operations*. *Nat Rev Neurosci*, 2014. **15**(4): p. 264-78.
- 703 47. Olshausen, B.A. and D.J. Field, *Emergence of simple-cell receptive field*  
704 *properties by learning a sparse code for natural images*. *Nature*, 1996.  
705 **381**(6583): p. 607-9.
- 706 48. Olshausen, B.A. and D.J. Field, *Sparse coding of sensory inputs*. *Curr Opin*  
707 *Neurobiol*, 2004. **14**(4): p. 481-7.
- 708 49. Coombs, S., et al., *The lateral line system*. Springer handbook of auditory  
709 research,. 2014, New York: Springer. xiv, 347 pages.
- 710 50. Liao, J.C., *Organization and physiology of posterior lateral line afferent neurons*  
711 *in larval zebrafish*. *Biol Lett*, 2010. **6**(3): p. 402-5.
- 712 51. St-Pierre, F., et al., *High-fidelity optical reporting of neuronal electrical activity*  
713 *with an ultrafast fluorescent voltage sensor*. *Nat Neurosci*, 2014. **17**(6): p.  
714 884-9.
- 715 52. Ji, N., D.E. Milkie, and E. Betzig, *Adaptive optics via pupil segmentation for*  
716 *high-resolution imaging in biological tissues*. *Nat Meth*, 2010. **7**(2): p. 141-  
717 147.
- 718 53. Wang, K., et al., *Rapid adaptive optical recovery of optimal resolution over*  
719 *large volumes*. *Nat Meth*, 2014. **11**(6): p. 625-628.
- 720 54. Wang, K., et al., *Direct wavefront sensing for high-resolution in vivo imaging in*  
721 *scattering tissue*. *Nature Communications*, 2015. **6**: p. 7276.
- 722

723

## 724 **Acknowledgements**

725 We thank Misha B. Ahrens for the zebrafish lines. We thank Yong Jiang, Tongzhou Zhao,

726 WenKai Han, Shenqi Fan for assistance in building the 3D tracking system, real time  
727 behavioral analysis, and larval zebrafish experiments. We thank Dr. Bing Hu and Dr. Jie  
728 He for his support in zebrafish handling and helpful discussions.  
729

730 **Videos:**

731

732 **Video 1| Whole brain functional imaging of larval zebrafish under light stimulation**

733 Whole brain XLFM imaging of a 5 dpf agarose-embedded larval zebrafish expressing

734 nucleus-localized GCamp6f (huc:h2b-gcamp6f). Light stimulation was introduced at time

735 point  $t = 0$ . Whole brain activity was recorded at 77 volumes/s.

736

737 **Video 2| Whole brain functional imaging of spontaneous activities of larval**

738 **zebrafish**

739 Whole brain XLFM imaging of a 5 dpf agarose-embedded larval zebrafish expressing

740 nucleus-localized GCamp6f (huc:h2b-gcamp6f). Spontaneous neural activity was

741 recorded at 0.6 volumes/s.

742

743 **Video 3| Whole brain functional imaging of spontaneous activities of larval**

744 **zebrafish**

745 Whole brain XLFM imaging of a 5 dpf agarose-embedded larval zebrafish expressing

746 cytoplasm-labeled GCamp6s (huc:gcamp6s). Spontaneous neural activity was recorded at

747 0.6 volumes/s.

748

749 **Video 4| Whole brain functional imaging of larval zebrafish under light stimulation**

750 Whole brain XLFM imaging of a 5 dpf agarose-embedded larval zebrafish expressing

751 cytoplasm-labeled GCamp6s (huc:gcamp6s). Light stimulation was introduced at time

752 point  $t = 0$ . Whole brain activity was recorded at 50 volumes/s.

753

754 **Video 5| Tracking of larval zebrafish during prey capture behavior at low resolution**

755 Tracking and real time kinematic analysis of larval zebrafish during prey capture  
756 behavior at low resolution. Recorded at 190 frames/s.

757

758 **Video 6| Tracking of larval zebrafish during prey capture behavior at high  
759 resolution**

760 Tracking and real time kinematic analysis of larval zebrafish during prey capture  
761 behavior at high resolution. Recorded at 160 frames/s.

762

763 **Video 7| Whole brain functional imaging of a freely swimming larval zebrafish  
764 under light stimulation**

765 Whole brain XLFM imaging of a 7 dpf freely swimming larval zebrafish expressing  
766 cytoplasm-labeled GCamp6s (huc:gcamp6s). Light stimulation was introduced at time  
767 point  $t = 0$ . Whole brain activities were recorded at 77 volumes/s and with a flashed  
768 excitation laser under 0.3 ms exposure time.

769

770 **Video 8| Whole brain functional imaging of a freely swimming larval zebrafish  
771 during prey capture behavior**

772 Whole brain XLFM imaging of an 11 dpf freely swimming larval zebrafish expressing  
773 cytoplasm-labeled GCamp6s (huc:gcamp6s). The entire process during which the larval  
774 zebrafish caught and ate the paramecium was recorded.

775

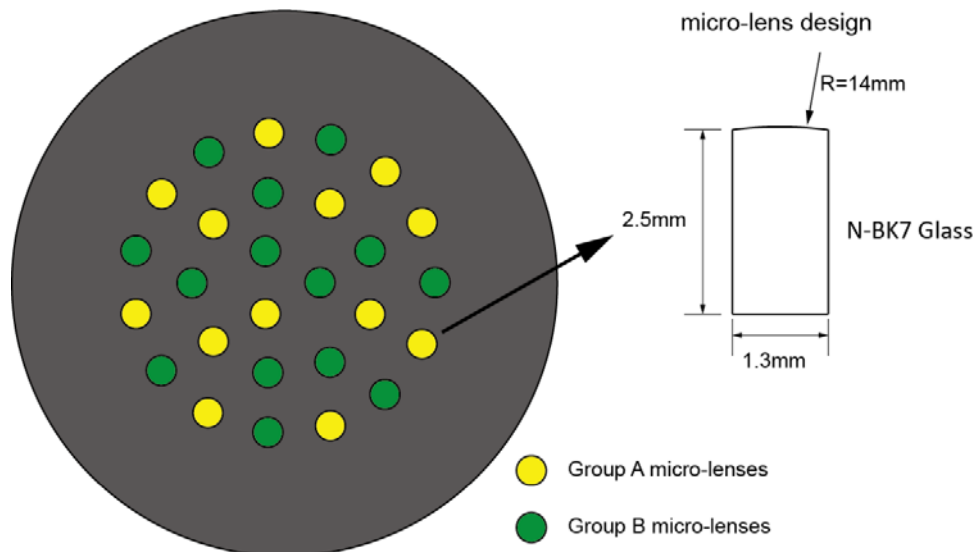
776 **Video 9| Whole brain functional imaging of a freely swimming larval zebrafish**

777 **during prey capture behavior**

778 Whole brain XLFM imaging of a 7 dpf freely swimming larval zebrafish expressing  
779 nucleus-localized GCamp6f (huc:h2b-gcamp6f). The entire process during which the  
780 larval zebrafish caught and ate the paramecium was recorded.

781

782 **Figure 1-figure supplement 1| Customized lenslet array**



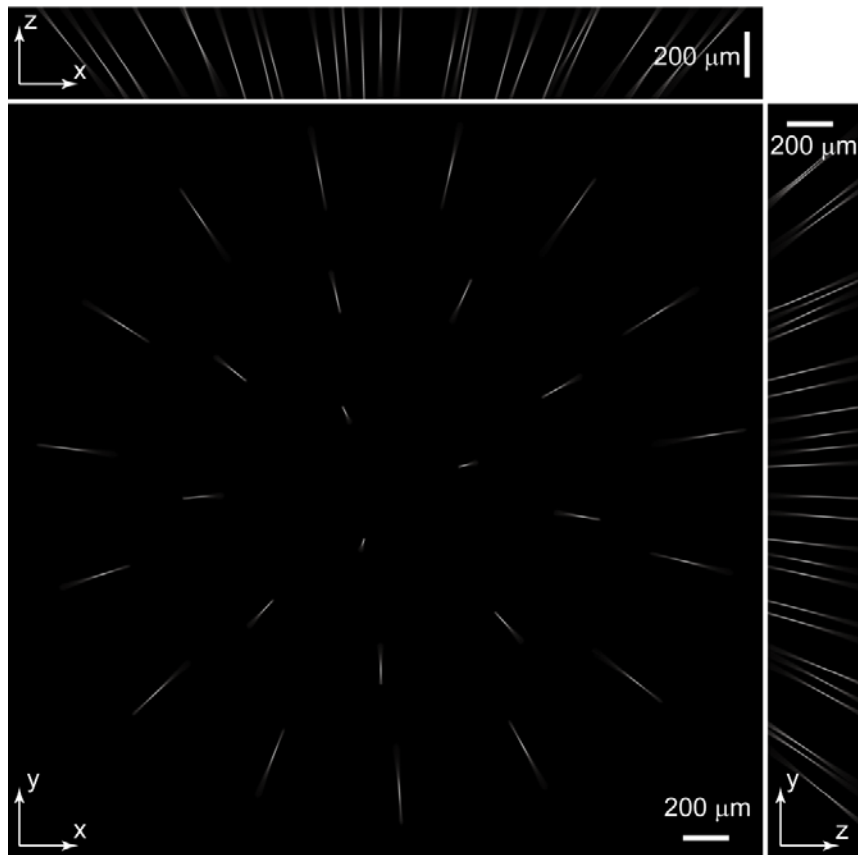
783

784 Customized lenslet array consisted of 27 customized micro-lenses (1.3 mm diameter, 26  
785 mm focal length) embedded in an aluminum plate with 27 drilled holes (1.3 mm diameter  
786 aperture on one side and 1 mm diameter aperture on the other side). Micro-lenses were  
787 divided into two groups (A or B), illustrated in yellow and green, respectively.

788



789 **Figure 1-figure supplement 2| Experimentally measured PSF of the whole imaging**  
790 **system**



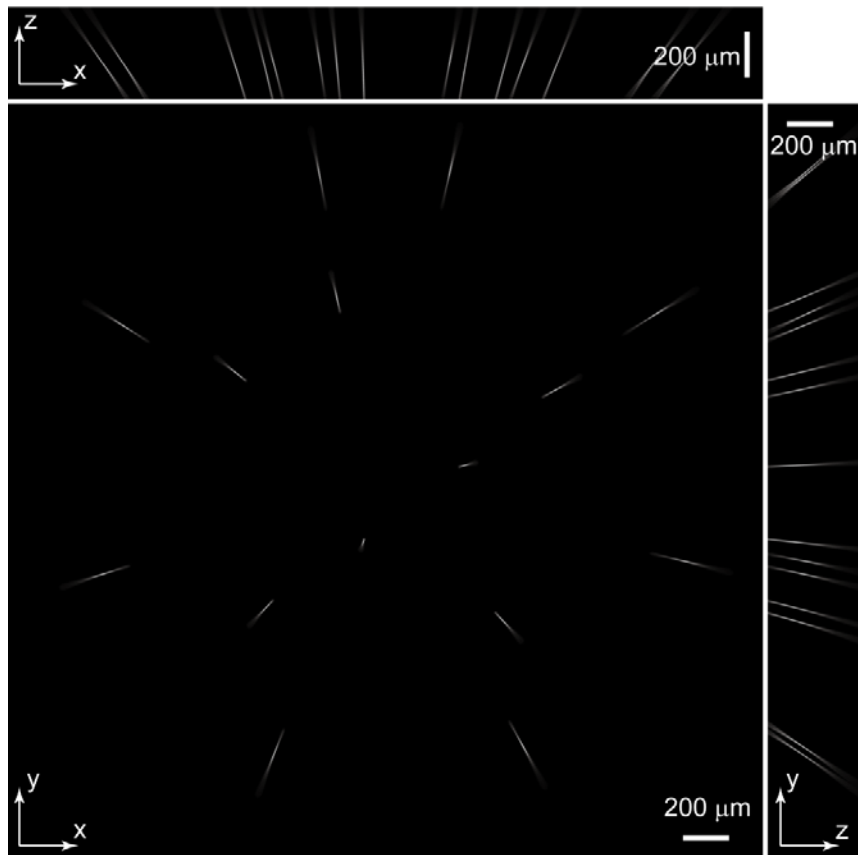
791

792 Maximum intensity projections (MIPs) of the measured raw PSF stack. The stack was

793  $2048 \text{ pixels} \times 2048 \text{ pixels} \times 200 \text{ pixels}$  with a voxel size of  $1.6 \mu\text{m} \times 1.6 \mu\text{m} \times 2 \mu\text{m}$ .

794

795 **Figure 1-figure supplement 3| PSF of Group A micro-lenses: PSF\_A**

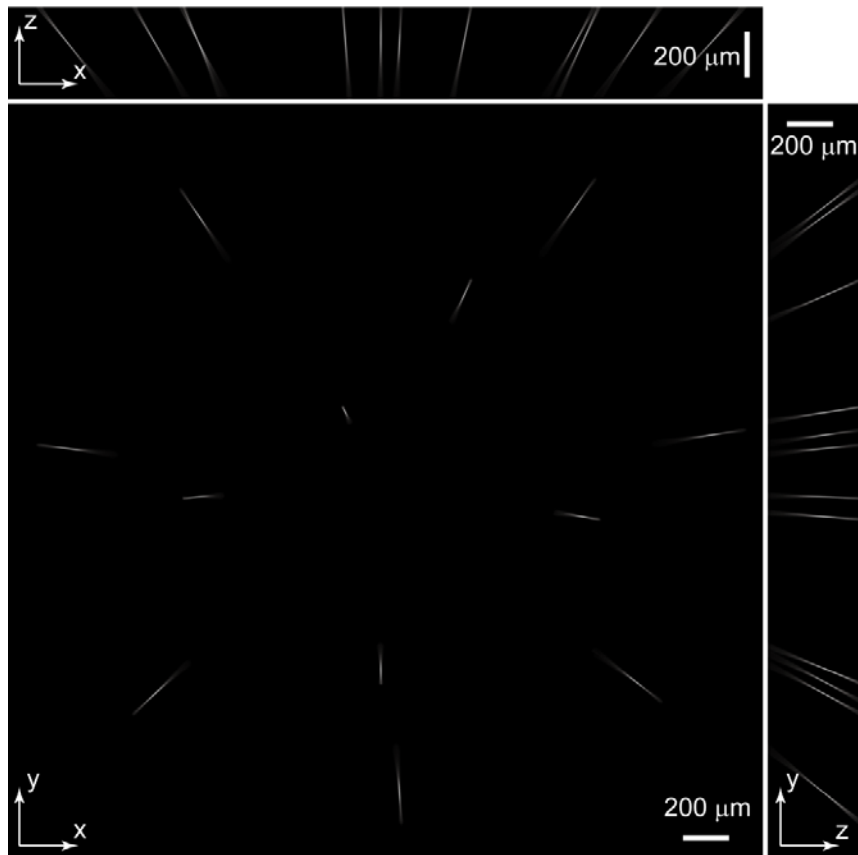


796

797 Maximum intensity projections (MIP) of PSF\_A. PSF\_A was extracted from  
798 experimentally measured PSF (Figure 1-figure supplement 2) according to individual  
799 micro-lens positions in group A.

800

801 **Figure 1-figure supplement 4| PSF of Group B micro-lenses: PSF\_B**

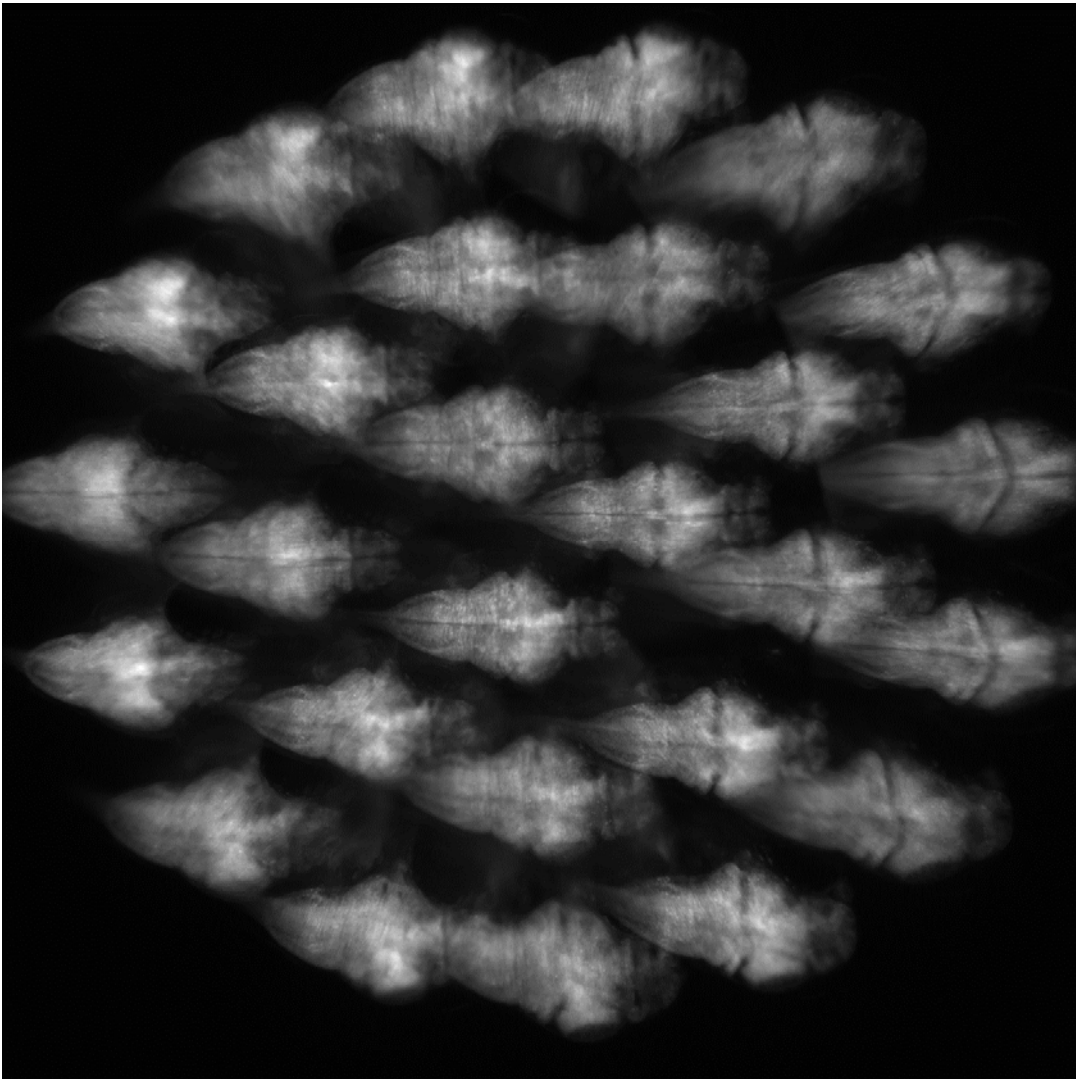


802

803 Maximum intensity projections (MIP) of PSF\_B. PSF\_B was extracted from  
804 experimentally measured PSFs (Figure 1-figure supplement 2) according to individual  
805 micro-lens positions in group B.

806

807 **Figure 1-figure supplement 5| Example of camera captured raw imaging data of**  
808 **larval zebrafish.**

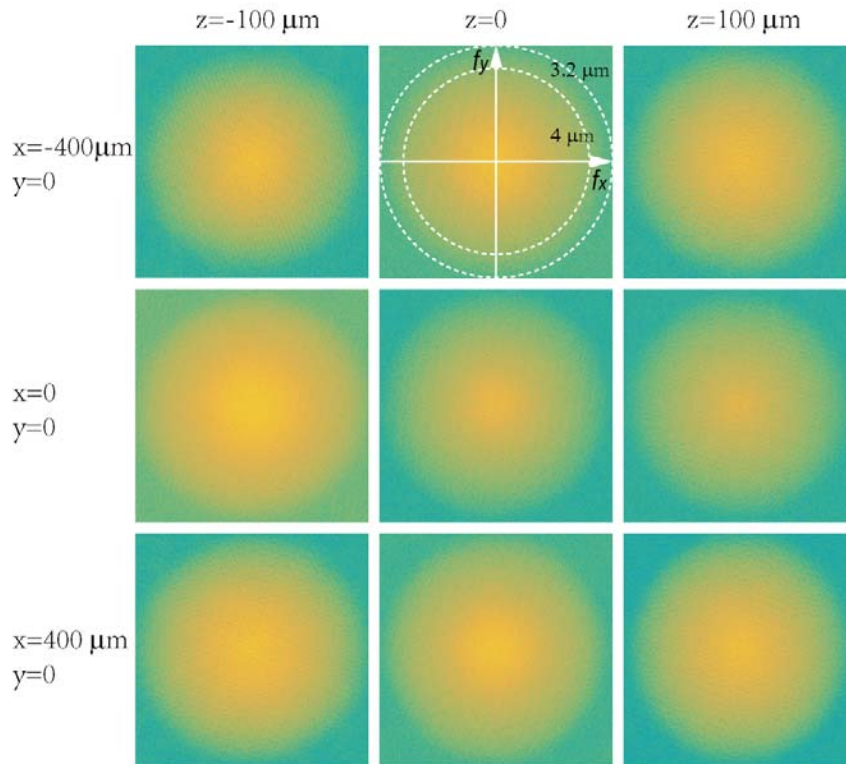


809

810 Raw fluorescence imaging data consisted of 27 sub-images of a larval zebrafish formed  
811 by 27 micro-lenses. Under the condition that the PSF is spatially invariant, which is  
812 satisfied apart from small aberrations, the algorithm can handle overlapping fish images.

813

814 **Figure 1-figure supplement 6| Characterization of in-plane resolution of micro-**  
815 **lenses**



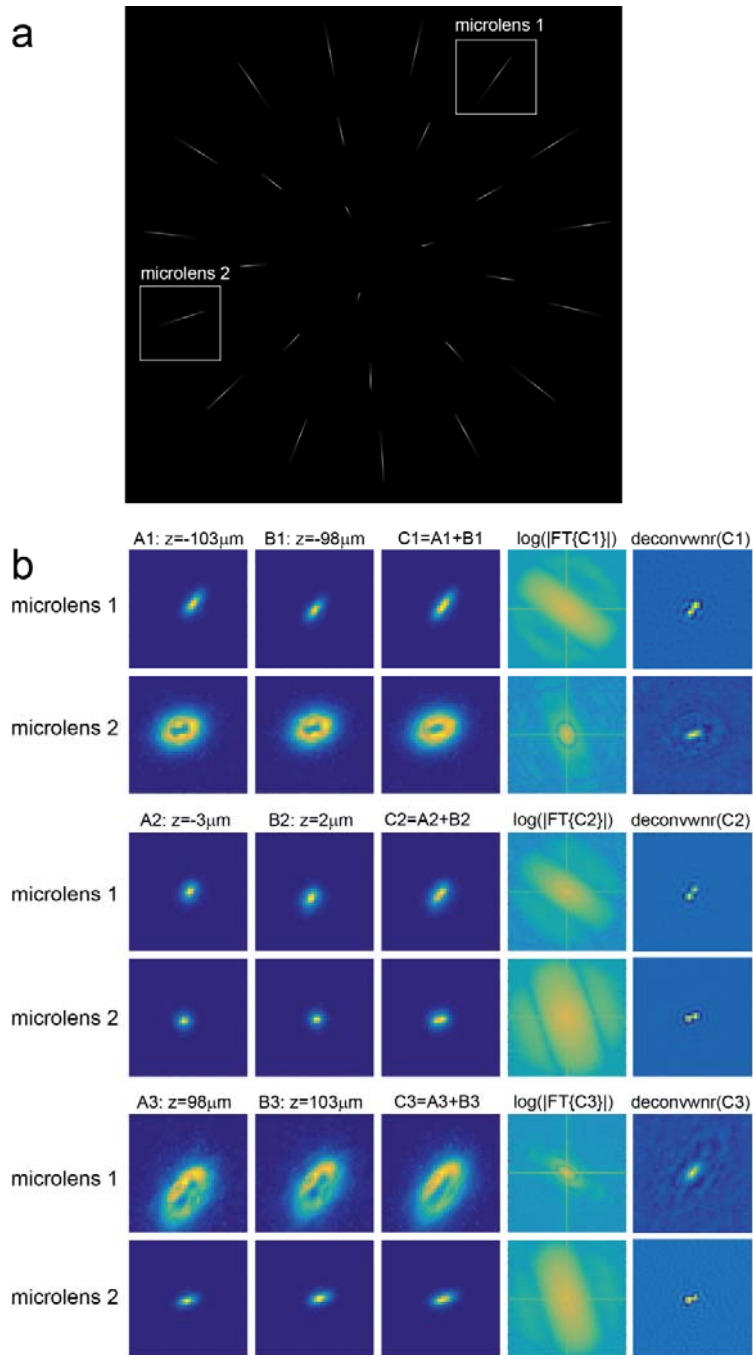
816

817 Fourier transforms of raw images of a 0.5- $\mu\text{m}$  diameter fluorescent particle placed at  
818 different locations ( $x = -400, 0, 400 \mu\text{m}$ ;  $z = -100, 0, 100 \mu\text{m}$ ) were plotted in log scales.

819 Dashed circles represent in-plane spatial frequency coordinates corresponding to spatial  
820 resolutions of 3.2  $\mu\text{m}$  and 4  $\mu\text{m}$ , respectively.

821

822 **Figure 1-figure supplement 7| Characterization of axial resolution of XLFM**  
823 **afforded by individual micro-lenses**



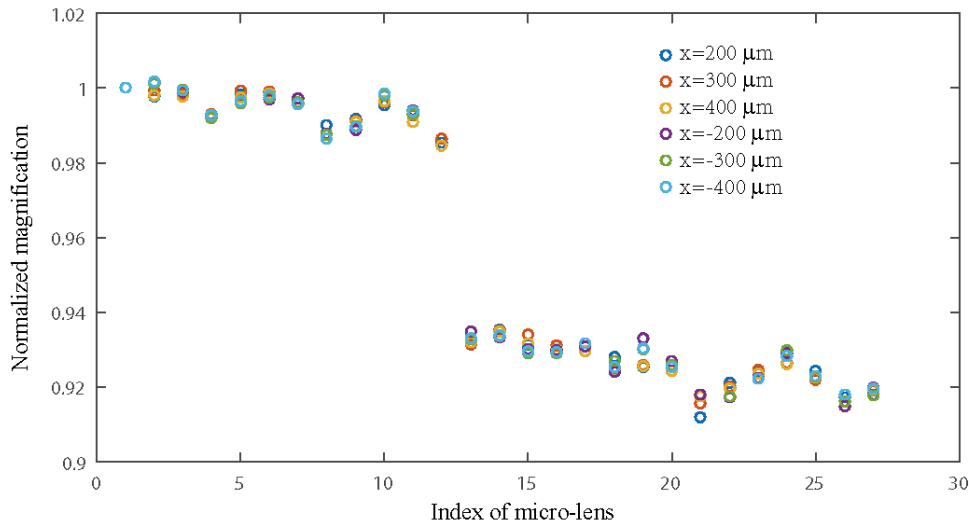
824

825 Characterization of axial resolution using a 0.5- $\mu$ m diameter bright fluorescent particle. (a)

826 Maximum intensity projection of an image stack consisting of the particle's fluorescent

827 images captured at different  $z$  positions. (b) Analysis of the images formed by micro-  
828 lenses 1 and 2, indicated by sub-regions in (a). The first and second columns are the  
829 particle's fluorescent images captured at different  $z$  positions separated by  $5 \mu\text{m}$ . The  
830 third column is the sum of columns 1 and 2. The fourth column is the Fourier analysis of  
831 column 3 using function:  $f(x) = \log(|\mathcal{F}(x)|)$ , where  $\mathcal{F}(x)$  represents the Fourier  
832 transform. The fifth column is the deconvolution of column 3 using Wiener filtering  
833 method. Experimentally measured images of the bead at different  $z$  positions ( $z = -100$   
834  $\mu\text{m}$ ,  $z = 0 \mu\text{m}$  and  $z = 100\mu\text{m}$ ) are employed as PSFs to deconvolve different images (C1,  
835 C2 and C3), respectively.  
836

837 **Figure 1-figure supplement 8| Characterization of magnification variation of micro-**  
838 **lenses in XLFM**

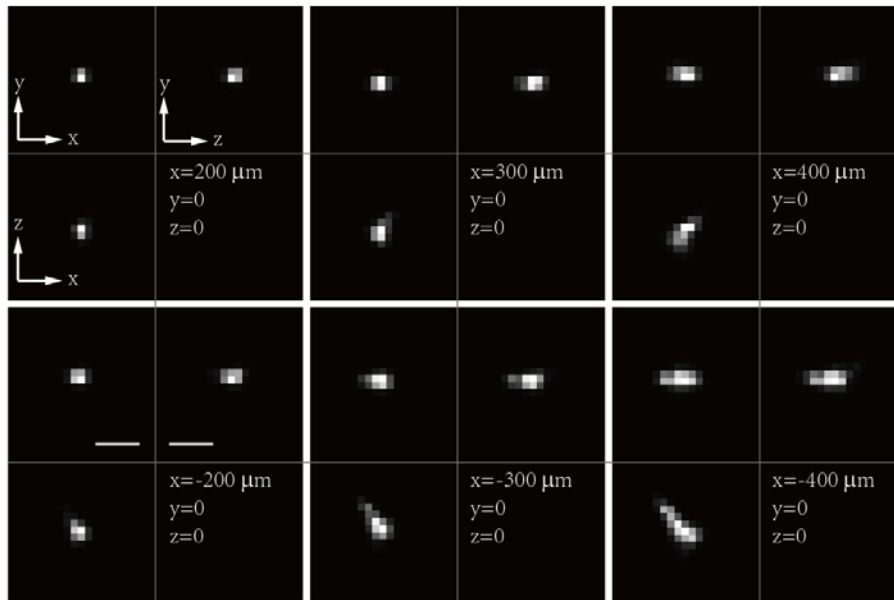


839

840 Magnifications of 27 micro-lenses were measured at different locations across the field of  
841 view. A fluorescent bead originally placed at the center of the field of view ( $x, y, z=0$ )  
842 was moved to six different locations ( $x = 200 \mu\text{m}, 300 \mu\text{m}, 400 \mu\text{m}, -200 \mu\text{m}, -300 \mu\text{m}, -$   
843  $400 \mu\text{m}, y = 0, z = 0$ ). Six classes of the bead's image shifts, represented by different  
844 colors, were measured. Each class consisted of 27 image shifts formed by 27 micro-  
845 lenses. Within each class, image shifts were normalized to the one from the first micro-  
846 lens. The first 12 micro-lenses and the rest formed two different groups of micro-lenses:  
847 group B and group A, consistent with Figure 1-figure supplements 3 & 4. The  
848 magnification variation of a single micro-lens across the field of view was small ( $< 0.3\%$ ),  
849 suggesting that the spatial invariance of individual micro-lens' PSF was well preserved  
850 across the field of view of  $\varnothing = 800 \mu\text{m}$ . The variation across different micro-lenses within  
851 one group (A/B) was more evident ( $\sim 2\%$ ), suggesting that the combined PSF from  
852 different micro-lenses was not perfectly spatially invariant.



853 **Figure 1-figure supplement 9| Resolution degradation due to focal length variation**  
854 **of micro-lenses**

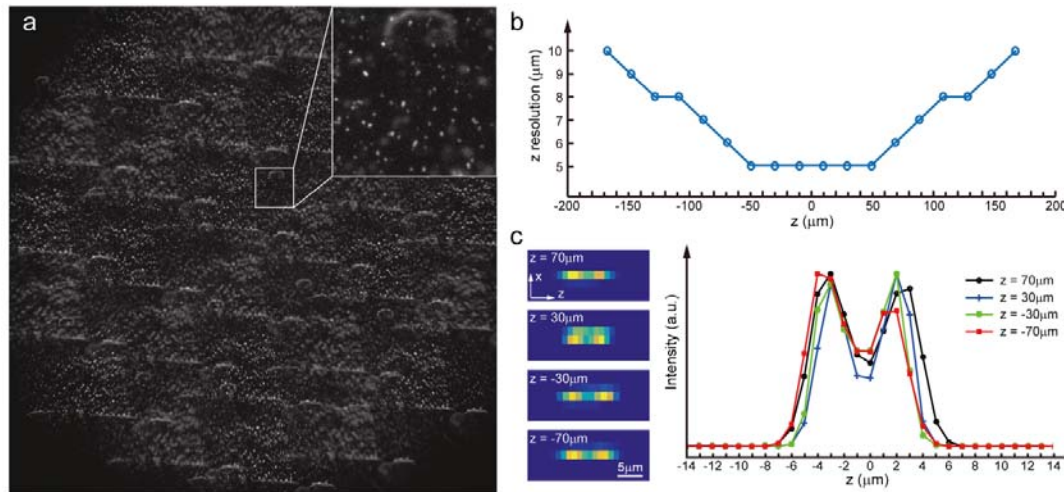


855

856 Maximum intensity projections (MIPs) of a reconstructed fluorescent bead positioned at  
857 different locations across the field of view. As the bead moved to the edge of the field of  
858 view, the reconstruction became distorted because the magnification variation of the  
859 micro-lenses led to spatial variance of total PSF. Scale bars are 10  $\mu\text{m}$ .

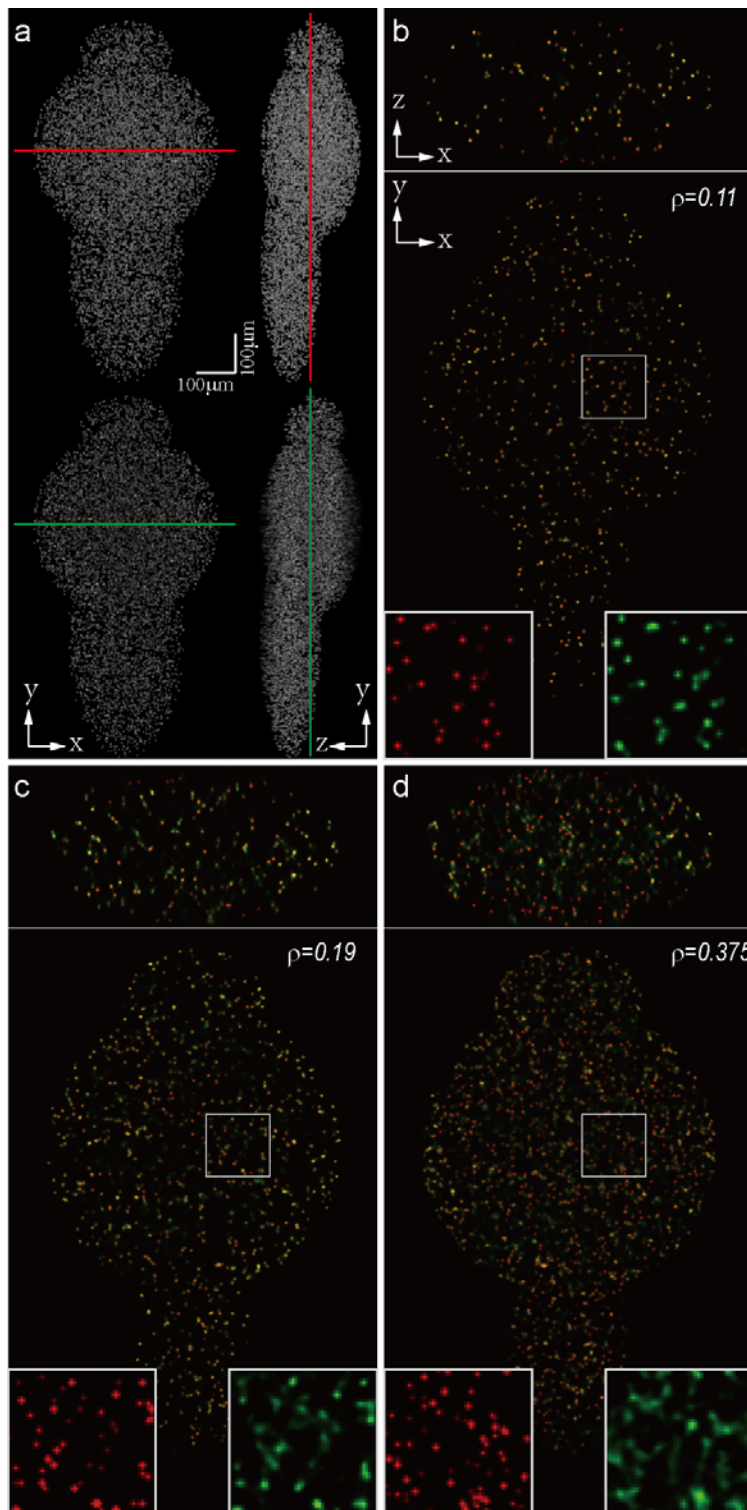
860

861 **Figure 1-figure supplement 10| Characterization of axial resolution of XLFM at low**  
862 **SNR**



863  
864 Characterization of axial resolution using densely packed fluorescent particles (0.5 μm in  
865 diameter) at low SNR. (a) Synthetic XLFM raw image (Methods) formed by two layers  
866 of fluorescent particles with different z positions. (b) Axial resolution at different depths  
867 characterized by the minimum separation of two particles in z, which can be resolved  
868 using the reconstruction algorithm (Methods). (c) Left, reconstructed examples of X-Z  
869 projections of two particles located at different z positions (-70 μm, -30 μm, 30 μm, 70  
870 μm) with different axial separations (6 μm, 5-μm, 5-μm, 6 μm); right, extracted intensity  
871 profiles of these examples.

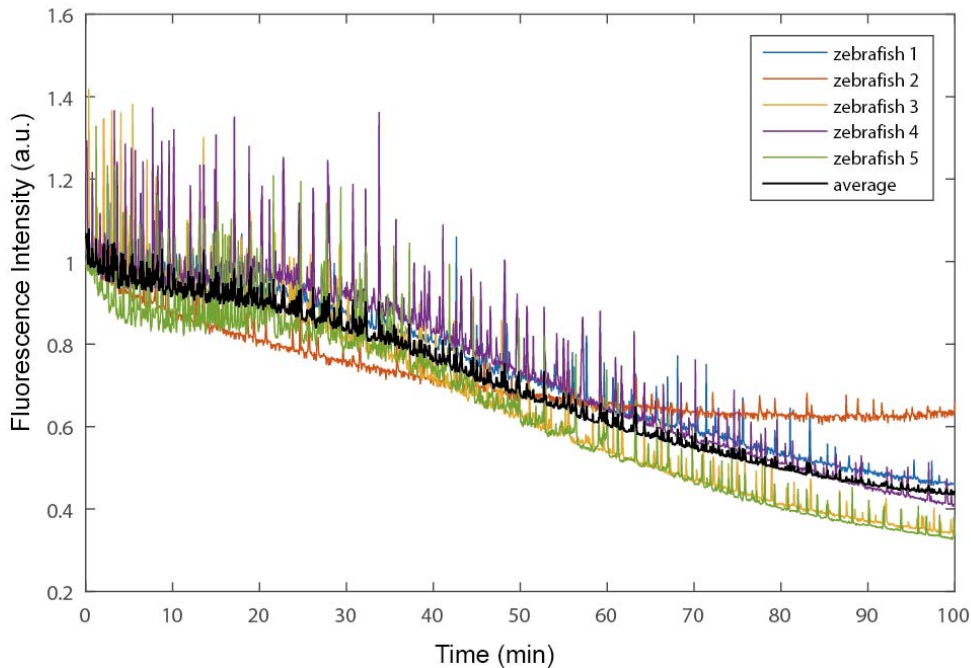
872 **Figure 1-figure supplement 11| Dependence of imaging resolution on the sparseness**  
873 **of the sample**



874

875 Characterization of the dependence of imaging resolution on the sparseness of the sample  
876 using computer simulation. (a) Maximum intensity projections (MIPs) of a numerically  
877 simulated (top) and reconstructed (bottom) larval zebrafish with randomly distributed  
878 active neurons. Red and green lines indicate positions where simulated (red) and  
879 reconstructed (green) cross-sections are compared. We assumed that the total number of  
880 neurons in the zebrafish brain is 80,000, and gradually increased the sparseness index  $\rho$ ,  
881 the fraction of neurons activated at a given frame. (b)–(d) Characterization of the  
882 reconstruction results for different  $\rho$ . Insets are magnified views of rectangular regions.  
883 Red and green dots are simulated and reconstructed neurons, respectively.  
884

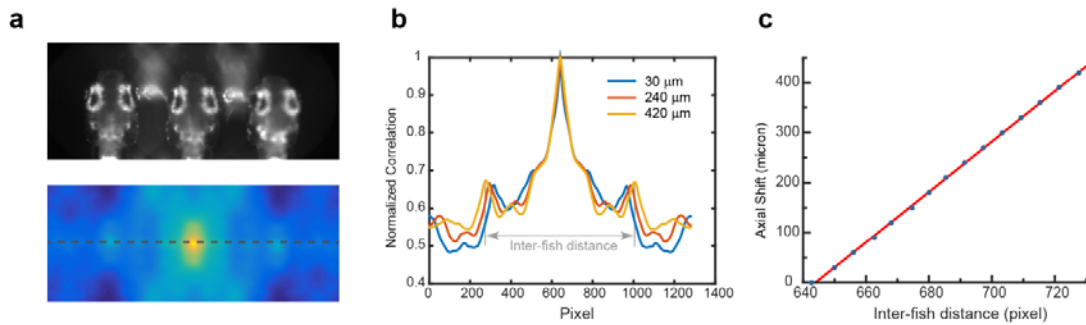
885 **Figure 1-figure supplement 12| Characterization of photobleaching in fluorescence**  
886 **imaging by XLFM**



887  
888 Photobleaching was characterized by a total fluorescence intensity change of five 5 dpf  
889 zebrafish larval with nucleus-localized GCamp6f (huc:h2b-gcamp6f). Each fish was  
890 embedded in 1% agarose and continuously exposed to 2.5 mW/mm<sup>2</sup> fluorescence  
891 excitation laser (488 nm) illumination. After ~100 min, corresponding to 300,000  
892 volumes with a volume rate of 50 volumes/s, total fluorescence intensity dropped to half  
893 of that at the starting point. Random spikes corresponded to spontaneous neural activity.  
894 Fish were alive and swam normally when they were relieved from the agarose after  
895 imaging.

896

897 **Figure 2-figure supplement 1| Characterization of the autofocus system**



898

899 (a) Autofocus camera behind a one-dimensional lenslet array captured triplet images of  
900 the fish head (up). Its autocorrelation function was computed (bottom). (b) Central line  
901 profile of the autocorrelation function was extracted and inter-fish distance was computed  
902 as local maximums in the autocorrelation function. (c) Axial shift of the fish head,  
903 calibrated by moving the piezo at a constant interval, changed linearly (red line) with  
904 inter-fish distance.

905

906

907

908

909

910

911

912

913

914

915

916

917 **Source Code File 1| Computer-Aided Design files of mounting plates for micro-**

918 **lenses array**

919

920 **Source Code File 2| Source code for XLFM reconstruction**

921

922 **Source Code File 3| Source code for Real-Time behavioral analysis**

923